Archives of Computational Methods in Engineering (2021) 28:713–751
https://doi.org/10.1007/s11831-020-09477-3

ORIGINAL PAPER

A Selection of Benchmark Problems in Solid Mechanics and Applied Mathematics

Jörg Schröder[1] · Thomas Wick[2] · Stefanie Reese[3] · Peter Wriggers[4] · Ralf Müller[5] · Stefan Kollmannsberger[6] · Markus Kästner[7] · Alexander Schwarz[1] · Maximilian Igelbüscher[1] · Nils Viebahn[1] · Hamid Reza Bayat[3] · Stephan Wulfinghoff[12] · Katrin Mang[2] · Ernst Rank[6] · Tino Bog[6] · Davide D'Angella[6] · Mohamed Elhaddad[6] · Paul Hennig[7] · Alexander Düster[8] · Wadhah Garhuom[8] · Simeon Hubrich[8] · Mirjam Walloth[9] · Winnifried Wollner[9] · Charlotte Kuhn[10] · Timo Heister[11]

Received: 21 July 2020 / Accepted: 17 August 2020 / Published online: 18 September 2020

Abstract
In this contribution we provide benchmark problems in the field of computational solid mechanics. In detail, we address classical fields as elasticity, incompressibility, material interfaces, thin structures and plasticity at finite deformations. For this we describe explicit setups of the benchmarks and introduce the numerical schemes. For the computations the various participating groups use different (mixed) Galerkin finite element and isogeometric analysis formulations. Some programming codes are available open-source. The output is measured in terms of carefully designed quantities of interest that allow for a comparison of other models, discretizations, and implementations. Furthermore, computational robustness is shown in terms of mesh refinement studies. This paper presents benchmarks, which were developed within the Priority Programme of the German Research Foundation 'SPP 1748 Reliable Simulation Techniques in Solid Mechanics—Development of Non-Standard Discretisation Methods, Mechanical and Mathematical Analysis'.

✉ Thomas Wick
thomas.wick@ifam.uni-hannover.de

Jörg Schröder
j.schroeder@uni-due.de

Stefanie Reese
stefanie.reese@rwth-aachen.de

Peter Wriggers
wriggers@ikm.uni-hannover.de

Ralf Müller
ram@rhrk.uni-kl.de

Stefan Kollmannsberger
stefan.kollmannsberger@tum.de

Markus Kästner
markus.kaestner@tu-dresden.de

Alexander Schwarz
alexander.schwarz@uni-due.de

Maximilian Igelbüscher
maximilian.igelbuescher@uni-due.de

Nils Viebahn
nils.viebahn@uni-due.de

Hamid Reza Bayat
hamid.reza.bayat@rwth-aachen.de

Stephan Wulfinghoff
swu@tf.uni-kiel.de

Katrin Mang
mang@ifam.uni-hannover.de

Ernst Rank
ernst.rank@tum.de

Tino Bog
tino.bog@tebis.com

Davide D'Angella
davide.dangella@tum.de

Mohamed Elhaddad
mohamed.elhaddad@tum.de

Paul Hennig
paul.hennig@tu-dresden.de

Alexander Düster
alexander.duester@tuhh.de

Wadhah Garhuom
wadhah.garhuom@tuhh.de

Simeon Hubrich
hubrich@tuhh.de

Mirjam Walloth
walloth@mathematik.tu-darmstadt.de

1 Introduction

Solving partial differential equations on complex geometries is perhaps one of the most important scientific achievement of the last decades. Analytical or manufactured solutions of such differential equations, e.g. from engineering or economics, is in most cases not available. Therefore, computer-aided numerical algorithms play an important role. At this point we mention that the rapid development of the available computing power contributes significantly to the success of these numerical methods. An end to this progress is currently not conceivable and becomes even more important due to the capabilities to address challenging multiphysics applications. Popular numerical methods are, for example, mesh-free methods, the finite volume method, finite differences, isogeometric analysis and—with possibly the greatest impact—the finite element method.

In this field, the German Priority Program 1748 (DFG SPP 1748) *Reliable Simulation Techniques in Solid Mechanics. Development of Non-standard Discretization Methods, Mechanical and Mathematical Analysis* is located. The main goal of this priority program was the development of modern non-conventional discretization methods based e.g. on mixed finite elements or discontinuous Galerkin formulations, including mathematical analysis for geometrically as well as physically non-linear problems in the areas of incompressibility, anisotropies and discontinuities to name a few. Typical problems especially in the field of geometric and material nonlinearities are for instance insufficient stress approximations due to unsuitable approximation spaces as well as weak convergence behavior due to stiffening effects or mesh distortions. Similar problems arise in crack or contact problems, where the local determination of discontinuities as well as their development play an important role in many fields of application.

This paper presents benchmark collections, which were compiled within the SPP 1748. The benchmarks were designed and shall serve as future reference for comparisons with other discretizations, nonlinear and linear solution algorithms. In the first two benchmarks we show results on hyperelastic and elasto-plastic problems at finite strains. Different (mixed) finite element technologies and p-FEM are used to obtain convergent results for certain displacement and stress values for Cook's membrane and an incompressible block problem. In the third benchmark problem (a thin as well as a thick plate) the convergence behavior was investigated. Here, both shell and continuum finite element technologies are used. The fourth benchmark concentrates on material interfaces that lead to high gradients or singularities. Therein, two discretization methods, finite elements and isogeometric analysis are compared. In the fifth benchmark, a phase-field method is applied for two- and three-dimensional propagating fractures. Lastly, again a phase-field fracture benchmark is provided. Therein, the fracture is subject to a constant pressure. For this setting, even manufactured solutions are known and taken as reference values. In all configurations, all necessary data are provided to reproduce our findings. These data include reference values, computations on mesh hierarchies and various quantities of interest.

Winnifried Wollner
wollner@mathematik.tu-darmstadt.de

Charlotte Kuhn
charlotte.kuhn@f07.uni-stuttgart.de

Timo Heister
heister@clemson.edu

[1] Abteilung Bauwissenschaften, Institut für Mechanik, Fakultät für Ingenieurwissenschaften, Universität Duisburg-Essen, Universitätsstr. 15, 45141 Essen, Germany

[2] Institut für Angewandte Mathematik, Leibniz Universität Hannover, Welfengarten 1, 30167 Hanover, Germany

[3] Institut für Angewandte Mechanik, Fakultät für Bauingenieurwesen, RWTH Aachen University, Mies-van-der-Rohe-Str. 1, 52074 Aachen, Germany

[4] Institut für Kontinuumsmechanik, Fakultät für Maschinenbau, Leibniz Universität Hannover, Appelstr. 11, 30169 Hanover, Germany

[5] Lehrstuhl für Technische Mechanik, Fachbereich Maschinenbau und Verfahrenstechnik, Technische Universität Kaiserslautern, Gottlieb-Daimler-Str., 67663 Kaiserslautern, Germany

[6] Lehrstuhl für Computergestützte Modellierung und Simulation, Ingenieurfakultät Bau Geo Umwelt, Technische Universität München, Arcisstr. 21, 80333 Munich, Germany

[7] Institut für Festkörpermechanik, Fakultät Maschinenwesen, Technische Universität Dresden, George-Bähr-Str. 3c, 01069 Dresden, Germany

[8] Numerische Strukturanalyse mit Anwendungen in der Schiffstechnik (M-10), Institut für Konstruktion und Festigkeit von Schiffen, Technische Universität Hamburg, Am Schwarzenberg-Campus 4 (C), 21073 Hamburg, Germany

[9] Fachbereich Mathematik, Technische Universität Darmstadt, Dolivo-Str. 15, 64293 Darmstadt, Germany

[10] Fakultät 7: Konstruktions-, Produktions- und Fahrzeugtechnik, Universität Stuttgart, Pfaffenwaldring 9, 70569 Stuttgart, Germany

[11] Mathematical and Statistical Sciences, O-110 Martin Hall, Clemson University, Clemson, SC 29634-0975, USA

[12] Institut für Materialwissenschaft, Technische Fakultät, Kiel University, Kaiser Str., 24143 Kiel, Germany

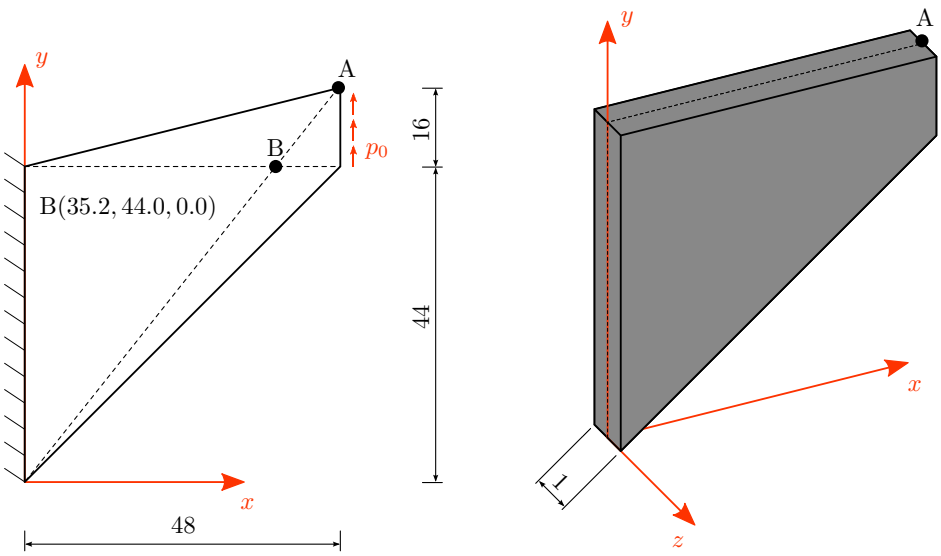

Fig. 1 Cook's membrane (all dimensions in mm)

2 Cook's Membrane: Hyperelasticity and Finite Elastoplasticity

In the first part of this benchmark, the Cook's membrane is investigated by applying a hyperelastic material model (Sect. 2.3) while in the second part a finite J_2 elastoplastic material model is used (Sect. 2.4). To this end, different element formulations are investigated by showing displacement and stress convergence studies. Furthermore, the locking effect due to the incompressibilty contraint is examined.

2.1 Geometry and Boundary Conditions

Cook's membrane, a tapered cantilever see Cook [1], combines bending and shearing. The left-hand side of the domain is clamped and a constant shear load in vertical direction is applied on the right-hand side. The thickness of the Cook's membrane is chosen to be 1 mm. The geometry and boundary conditions are illustrated in Fig. 1.

2.2 Element Formulations

Five different element formulations are used in this study. Two formulations are based on triangular (2D) or tetrahedral (3D) shaped elements. The first one applies a pure displacement based formulation with quadratic shape functions (in the following denoted as T_2) and the second one is a mixed formulation with an additional constant field for the pressure and volume dilatation (denoted with T_2P_0), see e.g. Boffi et al. [2]. The third and fourth formulation are based on hexahedral shaped elements with a first order polynomial interpolation of the displacements (represented by H_1) and a mixed formulation with a piecewise constant pressure field (denoted with H_1P_0), see e.g. Boffi et al. [2]. Furthermore, the three-dimensional problem is discretized also with hexahedral elements, which are used within a p-extension (p-FEM) based on the trunk space utilizing hierarchic shape functions, see Szabó and Babuška [3] and Düster et al. [4].

2.3 Cook's Membrane for Hyperelasticity

2.3.1 Hyperelastic Material Model

In the following we use two polyconvex strain-energy functions. The first function reads

$$\psi_1 = \frac{\mu}{2}(I_C - 3) + \frac{\lambda}{4}(J^2 - 1) - \left(\frac{\lambda}{2} + \mu\right)\ln J, \tag{2.1}$$

where λ and μ constitute the Lamé parameters, $J = \det \boldsymbol{F}$ the determinant of the deformation gradient $\boldsymbol{F}$ and $I_C = \mathrm{tr}\boldsymbol{C}$ the first principal invariant of the right Cauchy-Green tensor $\boldsymbol{C} = \boldsymbol{F}^T\boldsymbol{F}$, see e.g. Ciarlet [5]. The 2nd Piola Kirchhoff stress tensor $\boldsymbol{S} = 2\partial_{\boldsymbol{C}}\psi$ can be computed from the strain-energy function ψ_1 as follows

$$\boldsymbol{S} = \frac{\lambda}{2}(J^2 - 1)\boldsymbol{C}^{-1} + \mu(\boldsymbol{1} - \boldsymbol{C}^{-1}), \tag{2.2}$$

Table 1 Material parameters and applied load for ψ_1

Parameter	λ	μ	p_0
MPa	432.099	185.185	20

Table 2 Material parameters and applied load for ψ_2

Parameter	α	c_{10}	c_{01}	κ	p_0
MPa	3.67×10^{-3}	0.1788	0.1958	1000	0.25

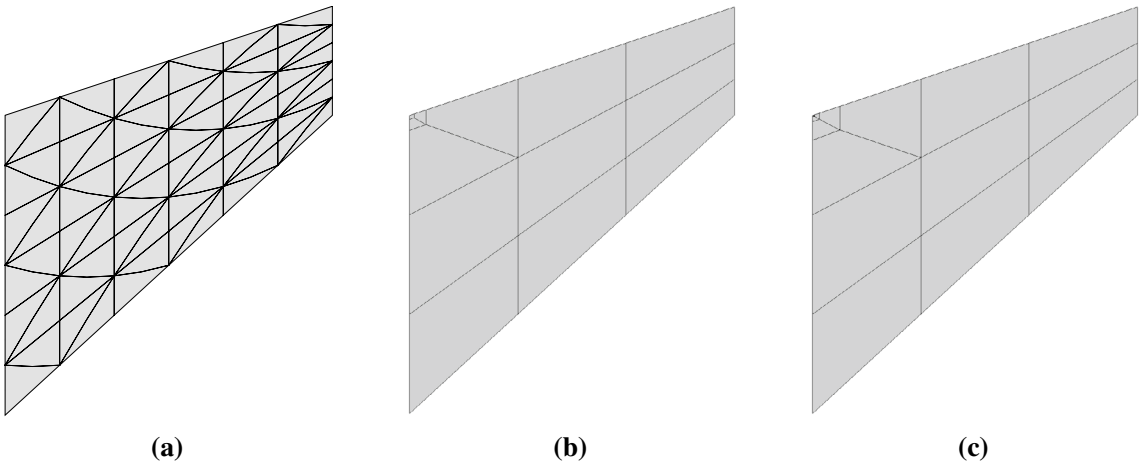

Fig. 2 Spatial discretization: **a** triangular mesh T_2 and T_2P_0 with 169 nodes **b** hexahedral mesh consisting of 13 elements with two refinements towards the singularity **c** hexahedral mesh consisting of 15 elements with three refinements towards the singularity

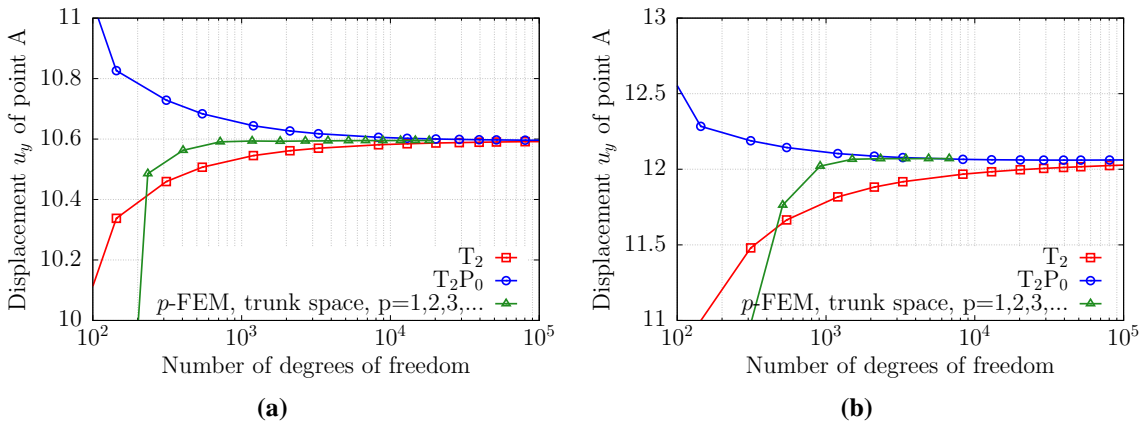

Fig. 3 Cook's membrane: **a** convergence of displacement u_y at point A for ψ_1 **b** convergence of displacement u_y at point A for ψ_2

here $\mathbf{1}$ denotes the second-order identity tensor. The material parameters (λ, μ) as well as the load p_0 are given in Table 1.

The second strain-energy function under consideration is based on a split into an isochoric $U(J)$ and unimodular $W(I_{\widetilde{C}}, II_{\widetilde{C}})$ part

$$\psi_2 = U(J) + W(I_{\widetilde{C}}, II_{\widetilde{C}}), \tag{2.3}$$

see Hartmann and Neff [6] and Netz et al. [7]. The principal invariants of the unimodular right Cauchy-Green tensor

$$\widetilde{\boldsymbol{C}} = (\det \boldsymbol{C})^{-1/3} \boldsymbol{C} \tag{2.4}$$

are given with

$$I_{\widetilde{C}} = \mathrm{tr}\widetilde{\boldsymbol{C}} \quad \text{and} \quad II_{\widetilde{C}} = \mathrm{tr}(\mathrm{Cof}\widetilde{\boldsymbol{C}}). \tag{2.5}$$

Following Hartmann and Neff [6] we choose the isochoric and unimodular parts of the strain energy as

$$U(J) = \frac{\kappa}{50}(J^5 + J^{-5} - 2) \tag{2.6}$$

and

$$\begin{aligned} W(I_{\widetilde{C}}, II_{\widetilde{C}}) =& \alpha(I_{\widetilde{C}}^3 - 27) + c_{10}(I_{\widetilde{C}} - 3) \\ &+ c_{01}(II_{\widetilde{C}}^{3/2} - 3\sqrt{3}). \end{aligned} \tag{2.7}$$

The 2nd Piola Kirchhoff stress tensor for ψ_2 can be computed as follows

Table 3 Convergence of the displacement component u_y of point A for ψ_1—for the p-FEM the hexahedral mesh with 13 elements was used with $p = 1, \ldots, 14$

DOFs	p-FEM	DOFs	T_2	T_2P_0
64	7.891541025	40	9.806907690	11.33745362
234	10.48552788	144	10.33773586	10.82618213
404	10.56281735	312	10.45943835	10.72849326
718	10.59074586	544	10.50672306	10.68358929
1176	10.59357161	1200	10.54536129	10.64401742
1817	10.59279059	3280	10.56978840	10.61771743
2680	10.59340608	8320	10.58101595	10.60584469
3804	10.59418029	12,960	10.58432907	10.60250393
5228	10.59459431	20,200	10.58680812	10.60010611
6797	10.59483724	39,480	10.58943610	10.59772491
8892	10.59500708	51,520	10.59020842	10.59707501
11,690	10.59512663	80,400	10.59124759	10.59625734
14,704	10.59521520	115,680	10.59191221	10.59578301
18,213	10.59528994			

Table 4 Convergence of the displacement component u_y of point A for ψ_2—for the p-FEM the hexahedral mesh with 15 elements was used with $p = 1, \ldots, 9$

DOFs	p-FEM	DOFs	T_2	T_2P_0
80	4.612355002	40	9.014811424	12.92227556
296	10.92119119	144	10.99908813	12.28386453
512	11.76326359	312	11.47965327	12.18887324
914	12.02094058	544	11.66479626	12.14388054
1502	12.06638464	1200	11.81742103	12.10409815
2327	12.07011195	3280	11.91767938	12.07732488
3440	12.06983163	8320	11.96768623	12.06585178
4892	12.07060838	12,960	11.98386546	12.06309408
6734	12.07068959	20,200	11.99686238	12.06151976
		39,480	12.01212534	12.06077186
		51,520	12.01710034	12.06087947
		80,400	12.02438600	12.06144138
		115,680	12.02957600	12.06218674

$$\begin{aligned} \boldsymbol{S} =& JU'(J)\boldsymbol{C}^{-1} + 2J^{-2/3} \\ & \Big((W_{,1} + W_{,2} I_{\widetilde{\boldsymbol{C}}})\boldsymbol{I} - W_{,2}\widetilde{\boldsymbol{C}} \\ & - \frac{1}{3}(W_{,1} I_{\widetilde{\boldsymbol{C}}} + 2W_{,2} II_{\widetilde{\boldsymbol{C}}})\widetilde{\boldsymbol{C}}^{-1} \Big) \end{aligned} \tag{2.8}$$

with

$$\begin{aligned} W_{,1} &= \partial W / \partial I_{\widetilde{\boldsymbol{C}}} = 3\,\alpha\, I_{\widetilde{\boldsymbol{C}}}^2 \quad \text{and} \\ W_{,2} &= \partial W / \partial II_{\widetilde{\boldsymbol{C}}} = c_{01}\,(3/2)\, II_{\widetilde{\boldsymbol{C}}}^{(1/2)}. \end{aligned} \tag{2.9}$$

The material parameters used for the second strain-energy function $(\alpha, c_{10}, c_{01}, \kappa)$ as well as the load p_0 are given in Table 2.

Furthermore, a Fortran77 code for the computation of the 2nd Piola Kirchhoff stress tensor and the material tangent $\mathbb{C} = 2\partial_{\boldsymbol{C}}\boldsymbol{S}$ will be provided online under (https://www.doi.org/10.5281/zenodo.4014897 (see also Korelc and Stupkiewicz [14])) with the subroutines:

```
SUBROUTINE mate1(v,F,\[Lambda],\[Mu],S,Cmat)
SUBROUTINE mate2(v,F,\[Kappa],\[Alpha],c10,c01,S,Cmat)
```

Here, the input parameters are the deformation gradient (`F` as 3×3 field) as well as the material parameters. The output parameters are the 2nd Piola Kirchhoff stress tensor (`S` as 3×3 field) and the material tangent (`Cmat` as $3 \times 3 \times 3 \times 3$ field). For further details on the material model and the solution of hyperelastic problems, the reader is referred to Hartmann and Neff [6], Düster et al. [8] and Wriggers [9].

2.3.2 Analysis for the 2D Plane Strain Case

In the following the convergence of the spatial discretization in terms of the vertical tip displacement u_y of the upper right node (point A, see Fig. 1) is compared. The meshes are uniformly refined by increasing the number of elements per edge. An exemplary mesh with triangular elements is depicted in Fig. 2a. Furthermore, for ψ_1 a mesh consisting of 13 hexahedral elements with two refinements towards the singularity is used and for ψ_2 a mesh with 15 hexahedral elements with three refinements, as depicted in Fig. 2b and c, respectively. The discretization is based on the trunk space utilizing 3D hierarchic shape functions. The plane strain conditions are enforced by suppressing the displacements in z-direction at the front ($z = 0.5$ mm) and reverse side ($z = -0.5$ mm) of the hexahedral meshes. In the following, we will consider both strain-energy functions ψ_1 and ψ_2. An uniform and isotropic increase of the polynomial degree $p = 1, 2, 3, \ldots$ of the shape functions yields the results depicted in Fig. 3a and b, which are plotted together with the displacements computed with the formulations T_2 and T_2P_0 for triangular elements. Furthermore, the results of the vertical displacement of point A are given in Tables 3 and 4.

Figure 4 shows the contour plot of the σ_{xx} stresses for the strain-energy function ψ_1. Here, the results of the T_2 and the T_2P_0 element are depicted in Fig. 4a and b, respectively. Figure 4c shows the contour plot of the σ_{xx} stresses for the p-FEM analysis using 13 hexahedral elements and the order of the Ansatz $p = 11$. In Fig. 5 the stress distribution for the strain-energy function ψ_2 is depicted. It shows the σ_{xx} stresses for the T_2 and the T_2P_0 element in Fig. 5a and b, respectively. To this end, the stress values are linearly

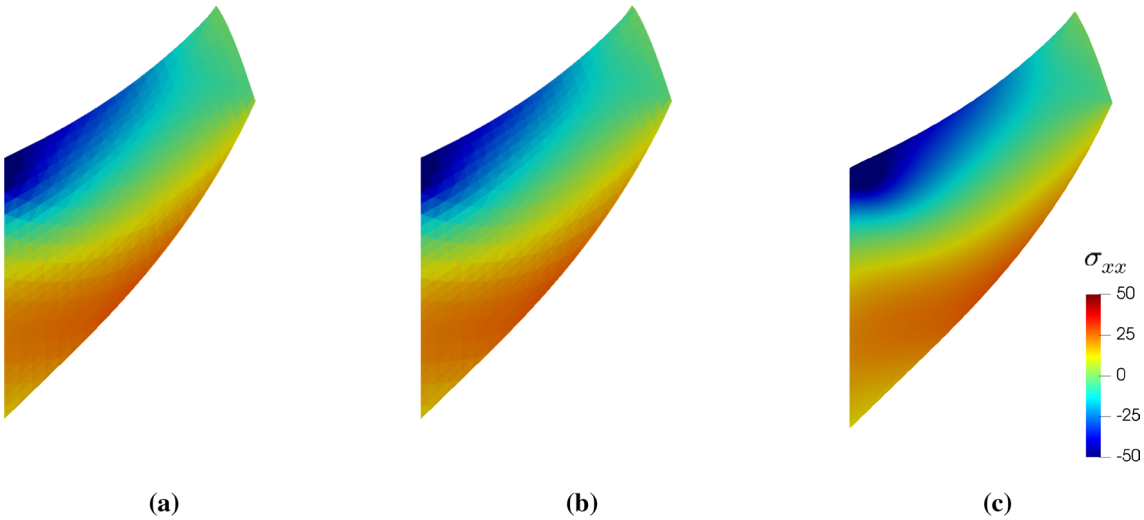

Fig. 4 Contour plot of the σ_{xx} stresses for ψ_1: **a** T_2 and **b** T_2P_0 with 4704 DOFs **c** p-FEM solution with 104 hexahedral elements and $p = 5$

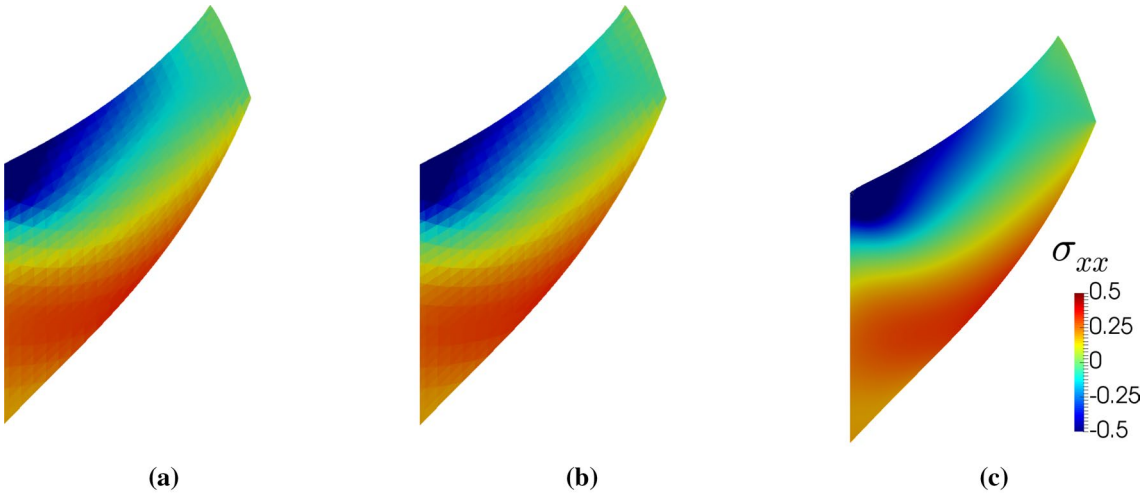

Fig. 5 Contour plot of the σ_{xx} stresses for ψ_2: **a** T_2 and **b** T_2P_0 with 4704 DOFs **c** p-FEM solution with 1026 hexahedral elements and $p = 9$

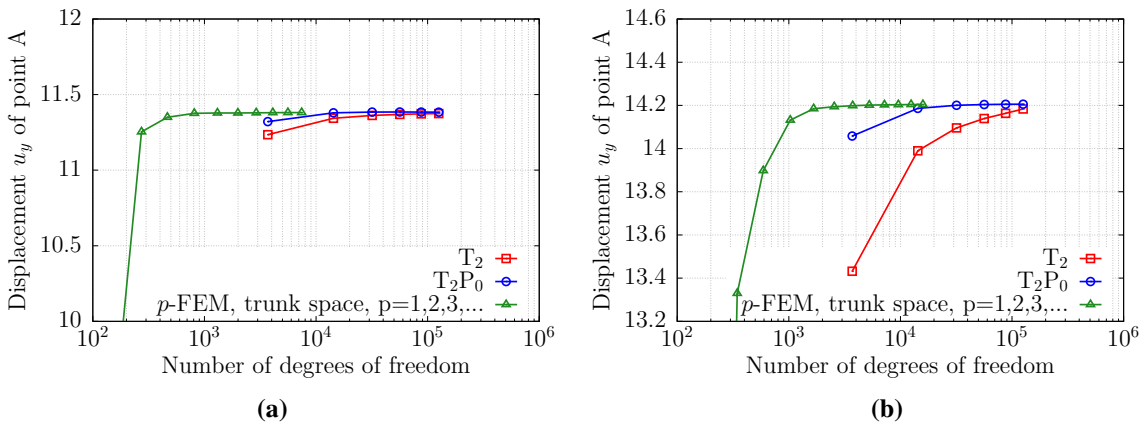

Fig. 6 Cook's membrane: **a** convergence of displacement u_y at point A for ψ_1 **b** convergence of displacement u_y at point A for ψ_2

Table 5 Convergence of the displacement component u_y at point A for ψ_1—for the p-FEM the hexahedral mesh with 13 elements was used with $p = 1, \ldots, 10$

DOFs	p-FEM	DOFs	T_2	T_2P_0
80	8.434841171	3696	11.23495734	11.32089255
273	11.25351064	14,304	11.34322180	11.37919731
466	11.35019765	31,824	11.36205916	11.38423863
811	11.37604404	56,256	11.36902825	11.38463195
1308	11.37813487	87,600	11.37244952	11.38429459
1996	11.37823068	125,856	11.37441412	11.38385850
2914	11.37933932			
4101	11.38030765			
5596	11.38083980			
7438	11.38113537			

Table 6 Convergence of the displacement component u_y at point A for ψ_2—for the p-FEM the hexahedral mesh with 15 elements was used with $p = 1, \ldots, 12$

DOFs	p-FEM	DOFs	T_2	T_2P_0
100	5.714955523	3696	13.43185080	14.05810063
345	13.32938972	14,304	13.98978503	14.18590622
590	13.89773326	31,824	14.09575681	14.20058990
1031	14.13196099	56,256	14.13898227	14.20412407
1668	14.18459516	87,600	14.16307381	14.20517718
2552	14.19396764	125,856	14.18356606	14.20539492
3734	14.19852431			
5265	14.20118387			
7196	14.20253217			
9578	14.20330321			
12,462	14.20377868			
15,899	14.20409718			

Table 7 Lamé's parameter λ and Poisson's ratio ν for ψ_1

λ in MPa	432.099	750	9260	92,600	926,000
ν	0.35000	0.40099	0.49020	0.49900	0.49990

Table 8 Bulk modulus κ and Poisson's ratio ν for ψ_2

κ in MPa	4	8	80	800	8000
ν	0.32614	0.40772	0.49023	0.49902	0.4999

extrapolated from the integration points to the nodal points. Stress oscillations can be recognized in the case of the displacement based element. The σ_{xx} stress distribution of the p-FEM solution is plotted in Fig. 5c. Here, a mesh with 1026 hexahedral elements is used and $p = 9$ to achieve a smooth solution of the stress distribution.

2.3.3 Analysis for the 3D Case

For the three-dimensional problem we choose the same constitutive model, geometry and boundary conditions analogous to the 2D setting. However, instead of plane strain conditions we consider stress-free out-of-plane surfaces, i.e. the front and reverse side of Cook's membrane are not constrained. Again, an uniform and isotropic p-refinement is performed utilizing the hexahedral mesh with 13 elements for ψ_1 and the hexahedral mesh with 15 elements for ψ_2 as depicted in Fig. 2b and c, respectively. The symmetry in z-direction is exploited by choosing one element layer of thickness 0.5 mm. In Fig. 6a and b the convergence of the displacement component u_y at point A is depicted together with the results obtained with the T_2 and T_2P_0 formulations for tetrahedral elements applying also a mesh layer thickness of 0.5 mm. The corresponding numbers are also depicted in Tables 5 and 6.

Influence of incompressibility: In this section, we investigate the influence of the incompressibility level on the convergence of the different discretizations. To this end, we keep the same material parameters and load as before and only change the Lamé's parameter λ for the first free energy function ψ_1 and the bulk modulus κ for the second free energy function ψ_2. The values of Poisson's ratio are approximated considering the corresponding relations for homogeneous isotropic linear materials, see Tables 7 and 8. Consequently, Poisson's ratio for ψ_1 is computed as

$$\nu = \frac{\lambda}{2(\lambda + \mu)} \tag{2.10}$$

and for ψ_2 as

$$\nu = \frac{3\kappa - 2G}{6\kappa + 2G}, \tag{2.11}$$

whereas according to Hartmann and Neff [6] the shear modulus is defined as

$$G = 54\alpha + 2c_{10} + 3\sqrt{3}c_{01}. \tag{2.12}$$

In order to investigate the influence of the increasing incompressibility level, we study the convergence of the tip displacements. The reference solutions of the tip displacement u_y at point A are computed by the p-FEM discretization using 13 elements for ψ_1 and 15 elements for ψ_2. The corresponding values are given in Tables 9 and 10. Figure 7 depicts the convergence of the normalized displacement $u_y/u_{y,\text{ref}}$ for both strain-energy functions ψ_1 and ψ_2 computed with the different finite element formulations.

Table 9 Reference tip displacement considering strain energy ψ_1

λ in MPa	432.099	750	9260	92,600	926,000
$u_{y,\text{ref}}$ in mm	11.38113537	11.15639736	10.78267246	10.74641606	10.74061099

Table 10 Reference tip displacement considering strain energy ψ_2

κ in MPa	4	8	80	800	8000
$u_{y,\text{ref}}$ in mm	15.10420474	14.67075231	14.24783555	14.20432703	14.20075829

2.4 Cook's Membrane for Elastoplasticity

In this section we use the same setup as depicted in Fig. 1. Furthermore, we consider only the 3D case.

2.4.1 Finite J_2 Elastoplastic Material Model

First, a short summary of the governing equations for the underlying material model will be given which is based on the J_2 flow theory of elastoplasticity for finite strain including a nonlinear isotropic hardening. For a detailed overview about the theory the interested reader is referred to Simo [10–12] and Simo and Miehe [13].

For the material model the deformation gradient $\boldsymbol{F}$ is decomposed into an elastic $\boldsymbol{F}_e$ and a plastic $\boldsymbol{F}_p$ part by applying a multiplicative split

$$\boldsymbol{F} = \boldsymbol{F}_e \boldsymbol{F}_p. \tag{2.13}$$

Assuming J_2 von Mises plasticity the plastic deformation only depends on the deviatoric part of the stress tensor. Based on the multiplicative split in Eq. (2.13) the elastic deformation gradient reads $\boldsymbol{F}_e = \boldsymbol{F}\boldsymbol{F}_p^{-1}$, thus, the elastic right Cauchy-Green tensor $\boldsymbol{C}_e$ can be formulated as

$$\boldsymbol{C}_e = \boldsymbol{F}_p^{-T} \boldsymbol{C} \boldsymbol{F}_p^{-1}, \tag{2.14}$$

and the elastic left Cauchy-Green tensor $\boldsymbol{b}_e$ as

$$\boldsymbol{b}_e = \boldsymbol{F}\boldsymbol{C}_p^{-1}\boldsymbol{F}^T, \tag{2.15}$$

where $\boldsymbol{C}_p = \boldsymbol{F}_p^T \boldsymbol{F}_p$ defines the plastic right Cauchy-Green tensor.

An isotropic compressible Neo-Hookean material behavior is assumed for the elastic part of the deformation utilizing the following strain-energy function

$$\begin{aligned}\psi_e =& \frac{\lambda}{4}\left(III_{\boldsymbol{C}_e} - 1 - \ln III_{\boldsymbol{C}_e}\right) \\ &+ \frac{\mu}{2}\left(I_{\boldsymbol{C}_e} - 3 - \ln III_{\boldsymbol{C}_e}\right).\end{aligned} \tag{2.16}$$

In Eq. (2.16), λ and μ define the Lamé constants and $I_{\boldsymbol{C}_e}$ and $III_{\boldsymbol{C}_e}$ denote the first and third invariant of the elastic right Cauchy-Green tensor $\boldsymbol{C}_e$ or the elastic left Cauchy-Green tensor $\boldsymbol{b}_e$ as follows

$$\begin{aligned} &I_{\boldsymbol{C}_e} = \text{tr}\boldsymbol{C}_e \quad \text{and} \quad III_{\boldsymbol{C}_e} = \det\boldsymbol{C}_e \quad \text{or} \\ &I_{\boldsymbol{b}_e} = \text{tr}\boldsymbol{b}_e \quad \text{and} \quad III_{\boldsymbol{b}_e} = \det\boldsymbol{b}_e. \end{aligned} \tag{2.17}$$

The 1st and 2nd Piola-Kirchhoff as well as the Cauchy and Kirchhoff stress tensors read

$$\begin{aligned} &\boldsymbol{P} = \frac{\partial \psi_e}{\partial \boldsymbol{F}_e}, \quad \boldsymbol{S} = 2\frac{\partial \psi_e}{\partial \boldsymbol{C}_e}, \\ &\boldsymbol{\sigma} = \frac{2}{J_e}\boldsymbol{F}_e \frac{\partial \psi_e}{\partial \boldsymbol{C}_e}\boldsymbol{F}_e^T, \quad \boldsymbol{\tau} = 2\frac{\partial \psi_e}{\partial \boldsymbol{b}_e}\boldsymbol{b}_e. \end{aligned} \tag{2.18}$$

The yield criterion of the plasticity model reads

$$\Phi(\boldsymbol{\tau}, \bar{\alpha}) = \sqrt{\frac{3}{2}\boldsymbol{s} : \boldsymbol{s}} - K(\bar{\alpha}) \quad \text{with} \quad \boldsymbol{s} = \boldsymbol{\tau} - \frac{1}{3}\text{tr}(\boldsymbol{\tau})\boldsymbol{1}. \tag{2.19}$$

In Eq. (2.19) $\bar{\alpha}$ denotes the hardening variable, $\boldsymbol{s}$ defines the deviatoric part of the Kirchhoff stress tensor $\boldsymbol{\tau}$, and $K(\bar{\alpha})$ describes the hardening which consists of a linear and an exponential part as follows

$$K(\bar{\alpha}) = Y_0 + H\bar{\alpha} + \left(Y_\infty - Y_0\right)\left(1 - e^{-\delta\bar{\alpha}}\right), \tag{2.20}$$

see e.g. Simo [12]. Here, Y_0 denotes the initial yield stress, H the linear hardening parameter, Y_∞ the saturation stress, and δ the hardening exponent. In accordance to Simo and Miehe [13], the evolution of the plastic flow as well as the internal variable reads

$$-\frac{1}{2}\mathcal{L}_v \boldsymbol{b}_e = \gamma \frac{\partial \Phi}{\partial \boldsymbol{\tau}}\boldsymbol{b}_e \quad \text{and} \quad \dot{\bar{\alpha}} = -\gamma \frac{\partial \Phi}{\partial K(\bar{\alpha})}. \tag{2.21}$$

Here, $\mathcal{L}_v \boldsymbol{b}_e$ denotes the Lie derivative of the elastic left Cauchy-Green tensor $\boldsymbol{b}_e$ and $\gamma \geq 0$ is the non-negative plastic multiplier. Based on the principle of maximum dissipation, this follows by enforcing stationarity conditions for the Lagrange functional, which is constructed as an optimization problem with the constraint condition ($\Phi = 0$), depending on the Dissipation inequality and the yield criterion in relation with γ.

Furthermore, following Korelc and Stupkiewicz [14] Eq. (2.15) can be inserted into the plastic flow formula in Eq. (2.21) to obtain,

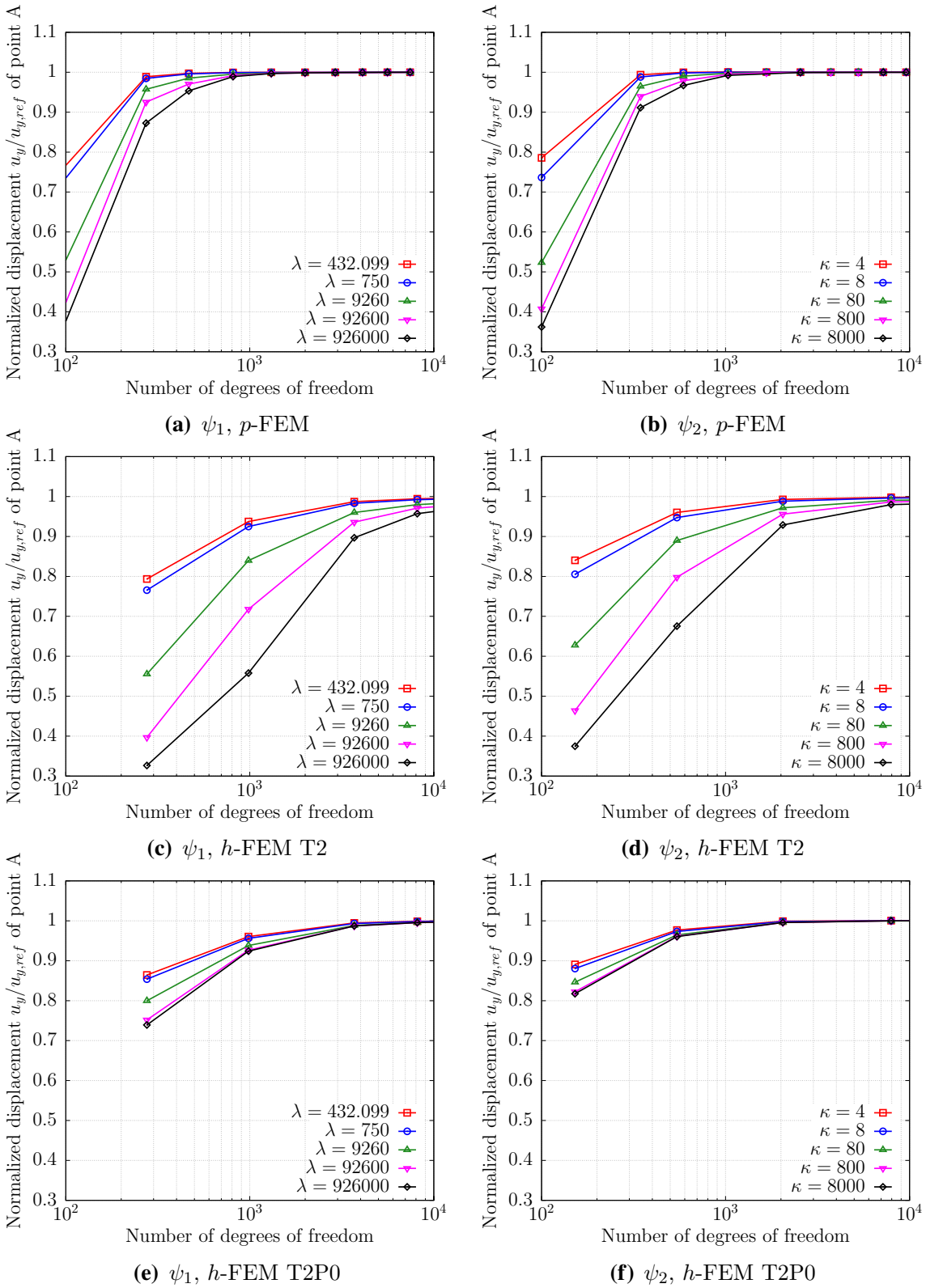

(a) ψ_1, p-FEM **(b)** ψ_2, p-FEM

(c) ψ_1, h-FEM T2 **(d)** ψ_2, h-FEM T2

(e) ψ_1, h-FEM T2P0 **(f)** ψ_2, h-FEM T2P0

Fig. 7 Locking behavior considering the normalized displacement $u_y/u_{y,\mathrm{ref}}$ of point A computed with the different finite element formulations

Table 11 Material parameters and applied load

λ	μ	Y_0	Y_∞	H	δ	p_0
110.743 MPa	80.194 MPa	450.0 MPa	715.0 MPa	129.24 MPa	16.93	350.0 MPa

Table 12 Convergence of the displacement component u_y at point A

DOFs	p-FEM	DOFs	H_1	H_1P_0	DOFs	T_2	T_2P_0
570	6.67213	630	7.08243	12.9631	921	11.5843	12.4056
2002	13.5791	2420	10.1830	13.3946	3524	13.4128	13.5667
3434	13.6521	9480	12.2640	13.5958	13,776	13.6750	13.7045
6040	13.6790	21,180	12.9299	13.6491	54,464	13.7016	13.7198
9799	13.6898	37,520	13.2212	13.6703	122,064	13.7080	13.7238
15,033	13.6985	70,730	13.4215	13.6860	–	–	–
22,051	13.7059	131,250	13.5360	13.6936	–	–	–
31,162	13.7070	–	–	–	–	–	–

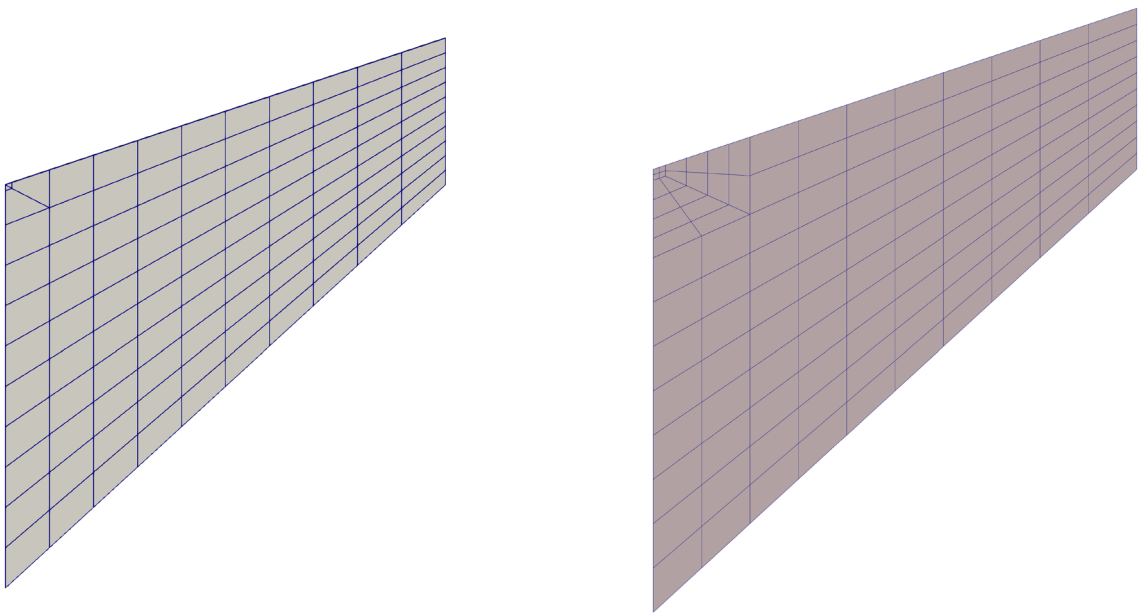

(a) **(b)**

Fig. 8 Spatial discretization: **a** a mesh consisting of 104 hexahedral elements with two refinements towards the singularity used for the p-FEM computations **b** the starting mesh for the H_1 and H_1P_0 formulations

Table 13 Convergence of the von Mises stress σ_{vM} at point B

DOFs	p-FEM	DOFs	H_1	H_1P_0	DOFs	T_2	T_2P_0
570	619.505	630	589.469	610.345	921	659.692	647.006
2002	599.683	2420	609.480	602.642	3524	615.844	609.117
3434	598.359	9480	614.556	598.425	13,776	598.334	597.072
6040	596.807	21,180	610.269	597.656	54,464	597.441	597.339
9799	597.214	37,520	606.473	597.616	122,064	596.884	596.798
15,033	597.327	70,730	602.896	597.434	–	–	–
22,051	596.939	131,250	600.484	597.310	–	–	–
31,162	597.078	–	–	–	–	–	–

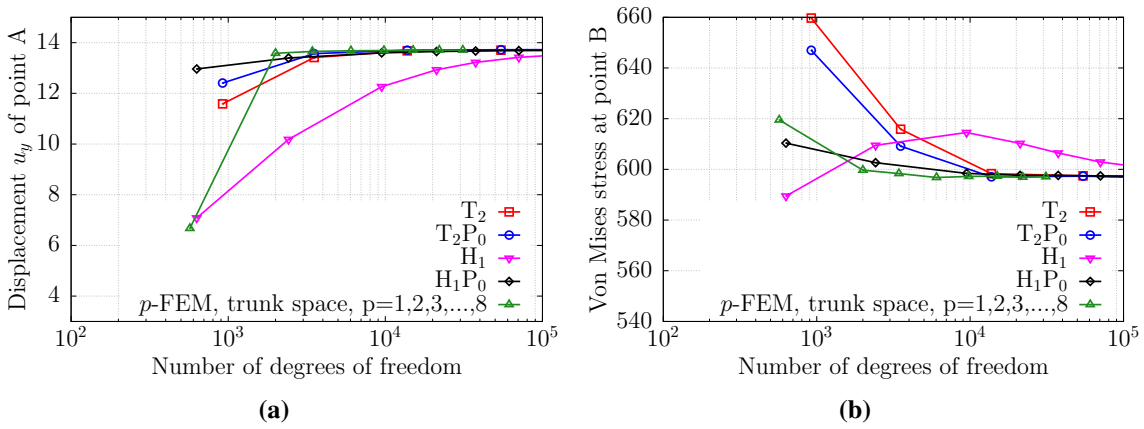

Fig. 9 Cook's membrane: **a** convergence of displacement u_y at point A **b** convergence of von Mises stress σ_{vM} at point B

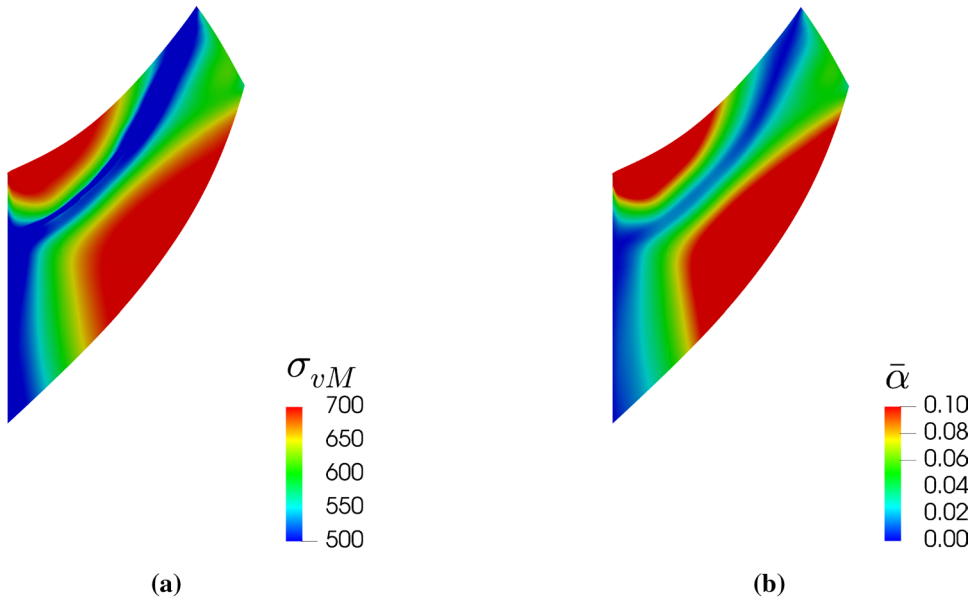

Fig. 10 Cook's membrane contour plots for p-FEM **a** von Mises stress σ_{vM} **b** equivalent plastic strain $\bar{\alpha}$, for $p = 6$ at the last load step

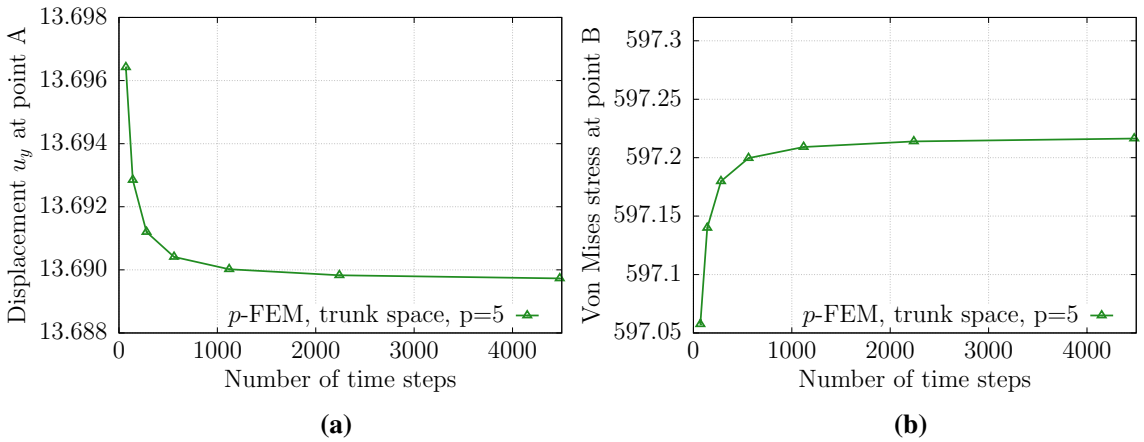

Fig. 11 Convergence study for different load steps using p-FEM, $p = 5$ **a** displacement u_y at point A **b** von Mises stress σ_{vM} at point B

Table 14 Convergence of the displacement component u_y at point A and the von Mises stress σ_{vM} at point B for different numbers of load steps using $p = 5$

Load steps	u_y	σ_{vM}
70	13.6964	597.058
140	13.6928	597.140
280	13.6912	597.180
560	13.6904	597.200
1120	13.6900	597.209
2240	13.6898	597.214
4480	13.6897	597.216

$$\dot{\boldsymbol{C}}_p^{-1} = -2\gamma \boldsymbol{F}^{-1} \frac{\partial \Phi}{\partial \boldsymbol{\tau}} \boldsymbol{F} \boldsymbol{C}_p^{-1}, \tag{2.22}$$

which is then used for the algorithmic treatment of the model. Finally, the material model is complemented by the Kuhn-Tucker conditions

$$\Phi \leq 0, \quad \gamma \geq 0, \quad \Phi\gamma = 0, \tag{2.23}$$

describing loading and unloading. For the integration of the internal variable $\dot{\bar{\alpha}}$, a backward Euler scheme is used. For the plastic variable $\dot{\boldsymbol{C}}_p$ an exponential map algorithm within an implicit time integration scheme is applied as follows

$$\bar{\alpha}_{n+1} = \bar{\alpha}_n + \Delta_t \gamma, \tag{2.24}$$

$$(\boldsymbol{C}_p^{-1})_{n+1} = \boldsymbol{F}_{n+1}^{-1} \exp\left[-2\Delta_t \gamma \frac{\partial \Phi_{n+1}}{\partial \boldsymbol{\tau}_{n+1}}\right] \boldsymbol{F}_{n+1} (\boldsymbol{C}_p^{-1})_n, \tag{2.25}$$

which was introduced by Weber and Anand [15] and Eterovic and Bathe [16]. Here, $\Delta_t \gamma$ denotes the increment of the plastic multiplier. The material parameters used in this benchmark as well as the load p_0 are given in Table 11.

As in the hyperelastic case the convergence of the spatial discretization in terms of the vertical tip displacement u_y of the upper right node (point A, see Fig. 1) is studied. As initial discretization a mesh consisting of 104 hexahedral elements with two refinements towards the singularity at the top left corner is used, as depicted in Fig. 8a. Again, we take advantage of symmetry and apply just one layer of elements of thickness 0.5mm. The starting mesh for the H_1 and H_1P_0 formulations is depicted in Fig. 8b, whereas in case of the T_2 and T_2P_0 each hexahedral element is subdivided into five tetrahedral elements, taking also advantage of symmetry in thickness direction. In the case of the h-FEM approach, the elements are uniformly refined in in-plane direction. In contrast, for the p-FEM the discretization is based on the trunk space utilizing hierarchic shape functions. An uniform and isotropic increase of the polynomial degree $p = 1, \ldots, 8$ of the shape functions yields the results depicted in Fig. 9a, which are plotted together with the displacements computed with the formulations T_2, T_2P_0, H_1 and H_1P_0. Furthermore, the results of the vertical displacement of point A are given in Table 12. Furthermore, a Fortran77 code for the computation of the 1st Piola Kirchhoff stress tensor and the material tangent $\mathbb{A} = \partial_{\boldsymbol{F}} \boldsymbol{P}$ will be provided online under (https://www.doi.org/10.5281/zenodo.4014897 (see also Korelc and Stupkiewicz [14])) with the subroutine:

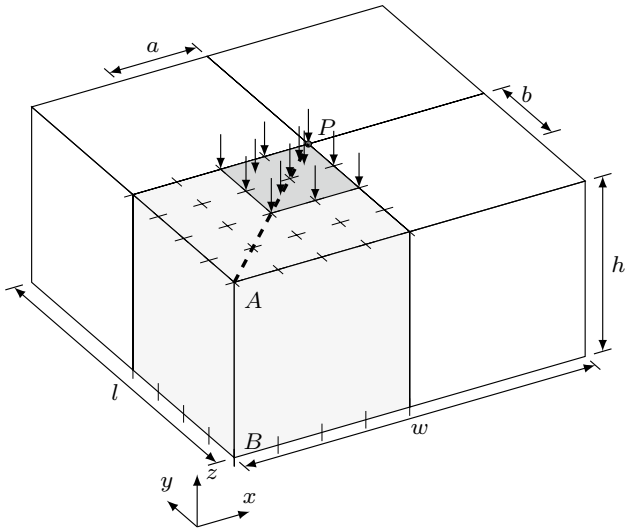

Fig. 12 Quasi-incompressible cube with partial load

Table 15 Dimensions of the problem

h in mm	w in mm	l in mm	a in mm	b in mm	q in MPa
50	100	100	25	25	3.0

```
SUBROUTINE mate(v,niter,MatIO,FIO,h1,SubIterationTolerance,P,Amat,h2,error)
```

Von Mises stress convergence: In the following, we study the convergence behavior of the von Mises stress. In doing so, we use the same meshes as in the previous section. In Fig. 9b the von Mises stress at point B is plotted over the number of degrees of freedom. The corresponding numbers are also depicted in Table 13. Figure 10a shows the contour plot for the von Mises stress σ_{vM} and Fig. 10b the equivalent plastic strain $\bar{\alpha}$ for $p = 6$ at the last load step.

Convergence study using different load steps: In the following we study the influence of the total number of load steps used to apply the load. To this end, the displacement u_y

Table 16 Material parameters

λ in MPa	μ in MPa
499.92568	1.61148

at point A and the von Mises stress σ_{vM} at point B are investigated. In doing so, we use the same mesh like in the previous section, as depicted in Fig. 8a applying a polynomial degree of $p = 5$ based on the trunk space utilizing hierarchic shape functions. In Fig. 11a and b, the displacements as well as the von Mises stress are plotted over the number of load steps chosen to apply the prescribed load. The corresponding numbers are also depicted in Table 14.

2.4.2 Remark

The software used in this study are AceGen and AceFEM (Korelc [17, 18], Korelc and Wriggers [19]) as well as in-house codes AdhoC^4 (Düster and Kollmannsberger [20]) and AdhoC++ which are jointly developed at the Technical University of Munich and the Hamburg University of Technology.

3 Incompressible Block Under Constant Partial Load

In this benchmark, a cube is subject to a vertical load on part of its upper surface. This benchmark poses two challenges for a FEM simulation in a geometrically non-linear setting:

- two line-singularities induced by a jump in the Neumann boundary condition which intersect in a point,
- almost incompressible material.

The benchmark allows to asses the performance of (high-order) displacement-based and mixed finite elements.

3.1 Geometry and Boundary Conditions

The system is depicted in Fig. 12.

Its dimensions are given in Table 15.

At the upper surface of the block, i.e. at $z = h$, displacements are fixed in both x- and y-direction. The bottom of the block, i.e. at $z = 0$, is fixed in z-direction.

Due to axial symmetry of loads and boundary conditions, computations were only carried out on the quarter of the block marked in light gray. To this end, homogeneous Dirichlet boundary conditions were additionally applied on the symmetry planes such that at $x = 0.5w$, displacements were fixed in x-direction and at $y = 0.5l$ displacements were fixed in y-direction.

Furthermore, the block is partially loaded with a constant surface load q on the area defined by a and b. The area in dark gray, thus, bears a mixed Dirichlet-Neumann boundary condition. These boundary conditions are chosen according to a similar test presented in Reese et al. [21].

3.2 Hyperelastic Material Model

We consider a deformation $\boldsymbol{\varphi}(\boldsymbol{X}, t)$ which maps points in the initial configuration to the current or deformed configuration. This deformation can be computed using the coordinates of the initial configuration and the displacement field: $\boldsymbol{\varphi}(\boldsymbol{X}, t) = \boldsymbol{X} - \boldsymbol{u}(\boldsymbol{X}, t)$. Using this deformation map, the deformation gradient can be computed as:

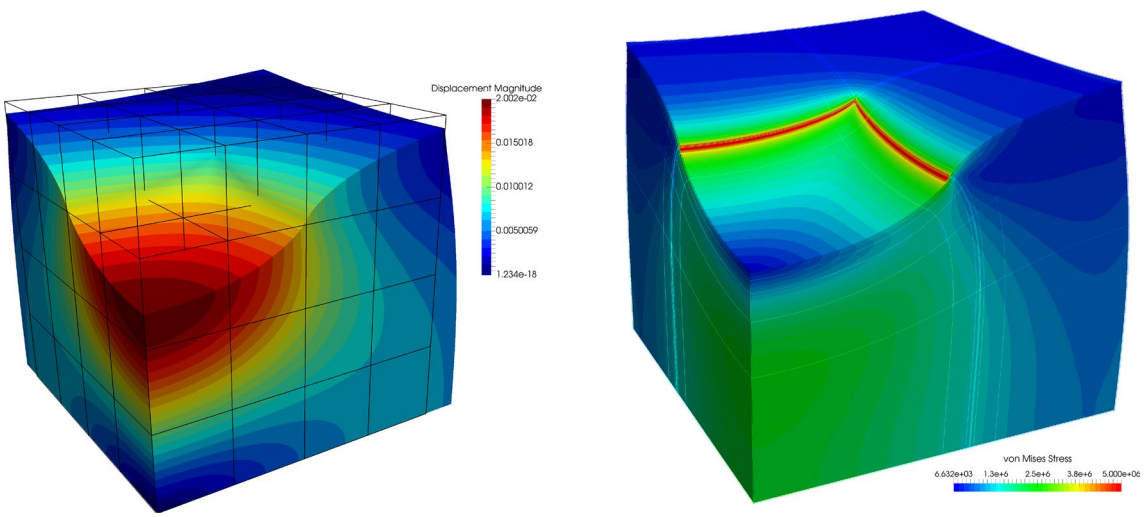

Fig. 13 Overall impression of results left: displacement magnitude on a fixed mesh of $4 \times 4 \times 4$ elements; right: von Mises stress on a $8 \times 8 \times 8$ mesh of $p = 8$, geometrically graded towards the traction boundary

Table 17 $|u_z(P)|$ for given element types, Dirichlet BC with DOF elimination

n_{dofs}	H1EI9	H1	H2	H1P0	O2P1	H1E9	TSCG
260	19.09	7.78	18.32	19.87	19.80	20.00	20.14
1800	19.98	13.17	19.54	20.02	19.93	20.05	20.10
13,328	20.01	17.54	19.98	20.01	19.97	0	20.03
102,432	20.00	19.52	20.01	20.00	19.98	0	20.01

The number of degrees of freedom for H1-elements is given. The results for all other elements are computed on the same uniform meshes with the same number of nodes as the corresponding H1-element which leads roughly to the same number of unknowns

Table 18 $|u_z(P)|$ for p-extension on a $4 \times 4 \times 4$ mesh, isotropic trunk space, Dirichlet conditions implemented with a penalty method

p	n_{dofs}	$\lvert u_z(P)\rvert$
1	375	7.656
2	1275	19.637
3	2175	19.998
4	3795	19.956
5	6135	19.986
6	9387	19.999
7	13,743	20.010
8	19,395	20.018
9	26,535	20.020
10	35,355	20.022

$$\begin{aligned} \boldsymbol{F} &= \text{Grad}\boldsymbol{\varphi}(\boldsymbol{X},t) = \text{Grad}(\boldsymbol{X} - \boldsymbol{u}(\boldsymbol{X},t)) \\ &= 1 + \boldsymbol{H}(\boldsymbol{X},t) \end{aligned} \tag{3.1}$$

where $\boldsymbol{H}(\boldsymbol{X},t)$ is the displacement gradient. The volume change J is given by the determinant of the deformation gradient: $J = \det \boldsymbol{F}$ and the right Cauchy-Green-tensor is defined by: $\boldsymbol{C} = \boldsymbol{F}^T\boldsymbol{F}$. Based on these quantities, the following isotropic strain energy function $W(\boldsymbol{\varphi})$ is used in this benchmark

$$W(\boldsymbol{\varphi}) = \frac{\mu}{2}(\text{tr}\boldsymbol{C} - 3 - 2\ln J) + \frac{\lambda}{2}(J-1)^2 \tag{3.2}$$

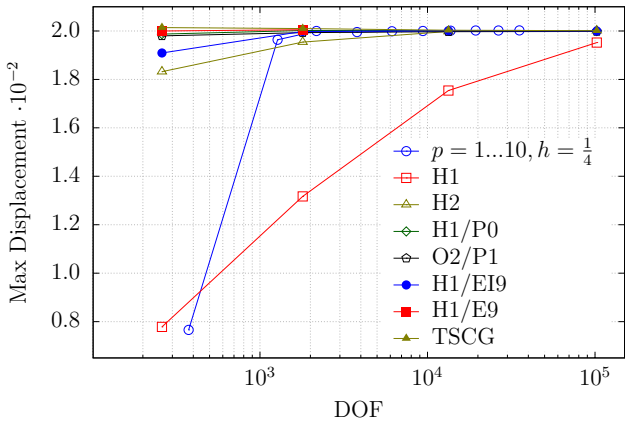

Fig. 14 Displacement at point P in z-direction ($u_z(P)$) for different element formulations and discretizations

The material parameters used in this benchmark are given in Table 16. They lead to a nearly incompressible material with a Poisson ratio of $\nu = 0.4983$.

3.3 Discretization and Results

An overall impression of the deformation is provided in Fig. 13 which depicts the displacement magnitude in the deformed configuration along with the wireframe of the corresponding hexahedral discretization in its initial configuration.

The convergence of the vertical displacement in z-direction at point P, $u_z(P)$, versus the degrees of freedom (DOF) of the discretization was investigated for the finite elements H1/EI9, H1, H2, H1/P0, O2/P1, H1/E9 (see e.g. Wriggers [9]) on regular meshes. Here $4 \times 4 \times 4$, $8 \times 8 \times 8$, $16 \times 16 \times 16$ and $32 \times 32 \times 32$ elements were used for the elements H1, H1/EI9, H1/P0 and H1/E9 with linear ansatz functions. For the hexahedral element H2 (27 nodes) and the tetrahedral element O2/P1with quadratic ansatz functions the number of elements was reduced such that the number of nodes was the same as for the elements with linear ansatz. The used elements are based on following ideas:

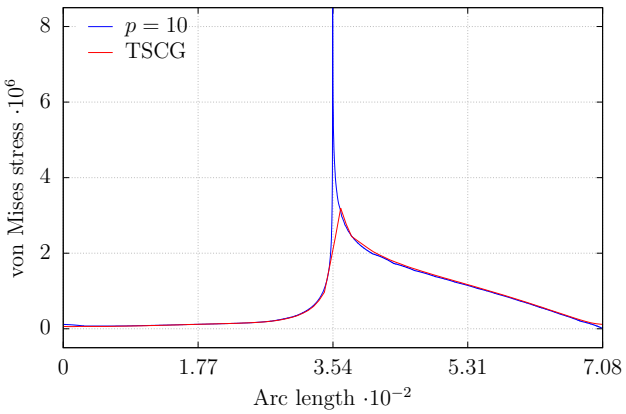

Fig. 15 Von Mises stress along diagonal from point P to point A on top face for the isotropic trunk space of order $p = 10$ on a $8 \times 8 \times 8$ mesh, geometrically graded towards the traction boundary and for a $64 \times 64 \times 64$ mesh of TSCG elements

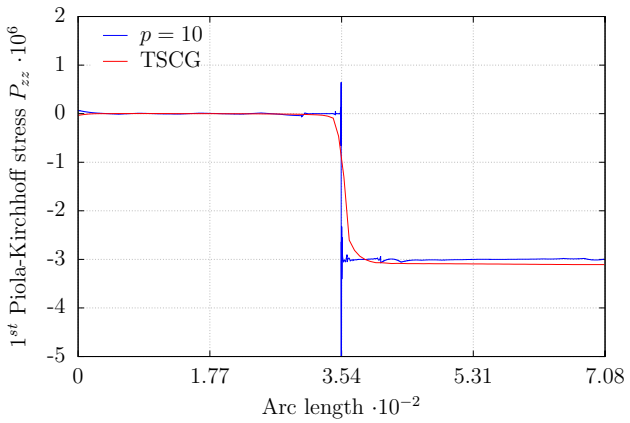

Fig. 16 1st Piola-Kirchhoff stress component P_{zz} along diagonal from point P to point A on top face for the isotropic trunk space of order $p = 10$ on a $8 \times 8 \times 8$ mesh, geometrically graded towards the traction boundary and for a $64 \times 64 \times 64$ mesh of TSCG elements

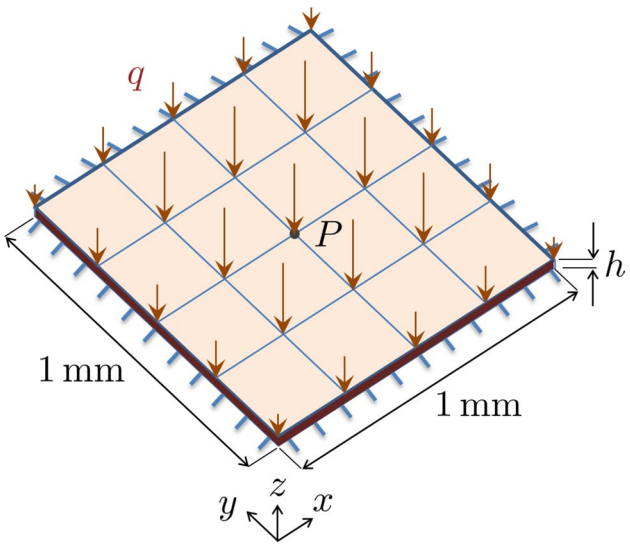

Fig. 17 Geometry, boundary conditions and loading of the thin plate

- **H1:** Classical hexahedral displacement based element with linear ansatz and $2 \times 2 \times 2$ nodes.
- **H2:** Classical hexahedral displacement based element with quadratic ansatz and $3 \times 3 \times 3$ nodes.
- **H1/E9:** Hexahedral mixed type ansatz with assumed enhanced strain fields and linear displacements. The element uses $2 \times 2 \times 2$ nodes and has 9 internal degrees of freedom related to the enhanced modes. These mode can be eliminated at element level using Schur complement techniques, details can be found in Simo and Armero [22].
- **H1/EI9:** Hexahedral mixed type ansatz with assumed enhanced strain fields and linear displacements, like H1/E9. However the enhanced strain modes are included here as a stabilization of a constant strain element, see Mueller-Hoeppe et al. [23].
- **H1/TSCG:** Hexahedral mixed type ansatz with 12 assumed enhanced strain fields and linear displacements. This element has a special stabilization to avoid hourglassing of H1/E9, see Korelc et al. [24].
- **H1/P0:** Hexahedral mixed element with linear ansatz for the displacement field and discontinuous constant pressure field at element level.
- **O2/P1:** Tetrahedral mixed element with quadratic ansatz for the displacement field and continuous linear pressure field.

The results are presented in Table 17 and Fig. 14. Since all these elements are developed using AceGen, see Korelc and Wriggers [19], they exhibit quadratic convergence within the Newton-Raphson solution algorithm. Both enhanced strain elements and the mixed O2/P1 and the H1/P0 elements are softer than the H2 element. All elements except the H1/E9 element converge practically to the same solution. For the H1/E9 element, solutions can only be obtained for the two coarsest meshes. For finer mesh resolutions the H1/E9 element depicts nonphysical hourglass instabilities.

Furthermore, a purely displacement based high-order finite element using the integrated Legendre basis functions described in Szabó et al. [25] (trunk space) was used and a p-extension was carried out on a fixed mesh with $4 \times 4 \times 4$ elements. The results are depicted in Fig. 14 and Table 18.

It can be observed that the pure displacement formulation locks for $p = 1$ on the h-refined meshes. This is expected for this nearly incompressible problem. However, locking may be controlled by increasing the order the finite elements as demonstrated by the curve given by a p-extension on a fixed mesh with $4 \times 4 \times 4$ elements.

For the high-order finite element using the integrated Legendre basis functions, additionally the stress component P_{zz} and the von Mises stress are measured along the diagonal line $A - P$ at $z = h$. The results on a discretization with $8 \times 8 \times 8$ pure displacement based elements of $p = 10$ are given in Figs. 15 and 16. The expected stress is zero at the homogeneous part of the Neumann boundary until it jumps to the value of the load q under the load surface. The discretization is only able to capture this jump approximately even though the discretization was geometrically propagated with a factor of 0.15 towards the singularity for this particular case.

Table 19 Deflection w_P at the central point of the plate ($a/h = 100$) for different number of elements in the thickness direction with 32 elements in the planar directions ($n_e = 32$)

n_z	1	2	4	8	16	32
Q1SP: w_P in µm	9.4099	8.4309	8.2019	8.1453	8.1312	8.1276
Q1STs: w_P in µm	8.1761	8.1417	8.1350	8.1335	8.1331	8.1330

4 Analysis of a Thin Plate

For the analysis of the complex thin geometries, such as shell and plate structures, various finite element methods have been developed to deliver accurate and efficient simulations. In this section, a study on the performance of three different element formulations is established for a thin plate. To this end, the thickness of the plate is varied from a thick to a very thin plate. Accordingly, two solid finite element methodologies as well as a solid-shell finite element technology are exploited.

4.1 Problem Definition

A square thin plate is to be investigated in this benchmark (see Korelc et al. [24]). It is clamped at all four sides (refer to Eq. 4.1) and is loaded by a distributed load of $q = 0.0002$ MPa. Geometry, boundary conditions and loading of the plate in 3D are illustrated in Fig. 17. The thickness of the plate h is a variable parameter for later investigations, whereas the side lengths a of the square are constant and equal to 1 mm.

The corresponding boundary conditions read as follows:

$$\begin{aligned} x = 0 &: u = v = w = 0, \\ x = a &: u = v = w = 0, \\ y = 0 &: u = v = w = 0, \\ y = a &: u = v = w = 0, \end{aligned} \tag{4.1}$$

where u, v and w are the displacements in x, y and z-directions, respectively.

4.2 Material Model

In the present work, a Neo-Hooke model for isotropic hyperelastic material behavior is applied. The material parameters are $\Lambda = 144.2307692$ MPa and $\mu = 96.1538$ MPa (corresponding to $E = 250$ MPa and $\nu = 0.3$). The strain energy function W is given by

$$\begin{aligned} W = &\frac{\mu}{2}(\mathrm{tr}\mathbf{C} - 3) - \mu \ln(\sqrt{\det\mathbf{C}}) \\ &+ \frac{\Lambda}{4}(\det\mathbf{C} - 1 - 2\ln(\sqrt{\det\mathbf{C}}), \end{aligned} \tag{4.2}$$

where $\mathbf{C} = \mathbf{F}^T\mathbf{F}$ is the right Cauchy-Green-tensor with $\mathbf{F}$ denoting the deformation gradient (see [26]).

The same plate is examined for the case of linear elasticity with the thickness $h = 0.01$ mm ($a/h = 100$) in the work of Bayat et al. [27] and Bayat et al. [28]. In the aforementioned studies, different conforming and non-conforming element formulations are compared in terms of rate of convergence with respect to the mesh refinement level.

4.3 Finite Element Technologies

Three different finite element methods are applied in this work. The first solid element formulation is the standard eight-node tri-linear Q1 brick element with eight Gauss points. Furthermore, an eight-node tri-linear solid element (Q1SP) with reduced integration (one Gauss point in the center of the element) and hourglass stabilization technique is applied. This element formulation is well-known for its performance in overcoming the problems concerned with shear as well as volumetric locking (please refer to Reese and Wriggers [26] and Reese [29]). Finally, an eight-node solid-shell (Q1STs) finite element with reduced integration (one integration point) within the shell plane and at least two integration points over the thickness is used (Schwarze and Reese [30, 31]). Similar to the Q1SP element formulation, this element benefits from enhanced assumed stains (EAS). However, in addition to the Q1SP element, the transverse shear and curvature thickness locking are additionally addressed by the employment of the assumed natural strain (ANS) concept.

4.4 Convergence Study

In order to investigate the convergence rate of different element formulations, the vertical displacement w_P at the point P on the upper side of the middle of the surface is investigated, see Fig. 17. To this end, different thicknesses h, different number of elements n_e and n_z in the planar directions (x and y) as well as in the out-of-plane direction (z) are considered. The ratio between the length and thickness of the plate (a/h) is varied by 20, 50, 100, 200, 500 and 1000 to cover a wide range of thick to thin plates.

Figure 18 shows the deformed plate with 10 times magnified displacements.

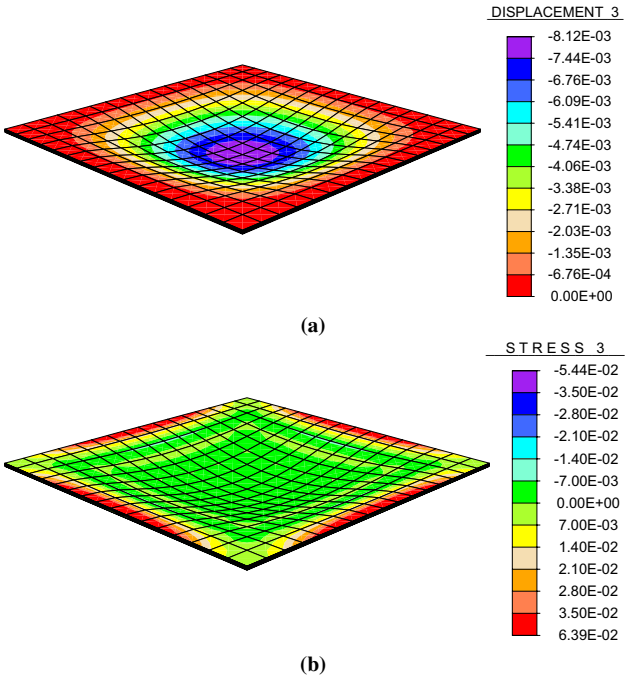

Fig. 18 **a** Displacement contour and **b** stress distribution of the deformed plate in z-direction (10 times magnified displacements). The geometrical aspect ratio $a/h = 100$ and the mesh size $n_e \times n_z = 16 \times 8$ are set

4.4.1 Influence of the Number of Elements in Thickness Direction

First, the influence of the number of elements in thickness direction on the displacement convergence rate is studied for the two finite element technologies Q1SP and Q1STs for the given aspect ratio $a/h = 100$. Figure 19 shows the influence of the number of elements (n_z) in thickness direction on the deflection w_P of the plate at the point P for different number of elements (n_e) in planar directions. In addition, the vertical displacements of the point P are given for the specific planar discretization $n_e = 32$ in Table 19.

According to Fig. 19, both solid and solid-shell element formulations converge with very few number of elements in thickness direction as long as enough number of elements in the planar directions are used. The difference between the performance of these two element formulations lies mainly in the application of only one element in the thickness direction. For a single element in z-direction, the Q1SP element formulation shows still a deviation from the converged solution. This is expected because one uses only one Gauss point in the thickness direction in this shell structure. The error of the Q1STs element technique for $n_z = 1$ is small. This is due to the fact that the latter approach benefits from possessing two or more integration points in the thickness direction.

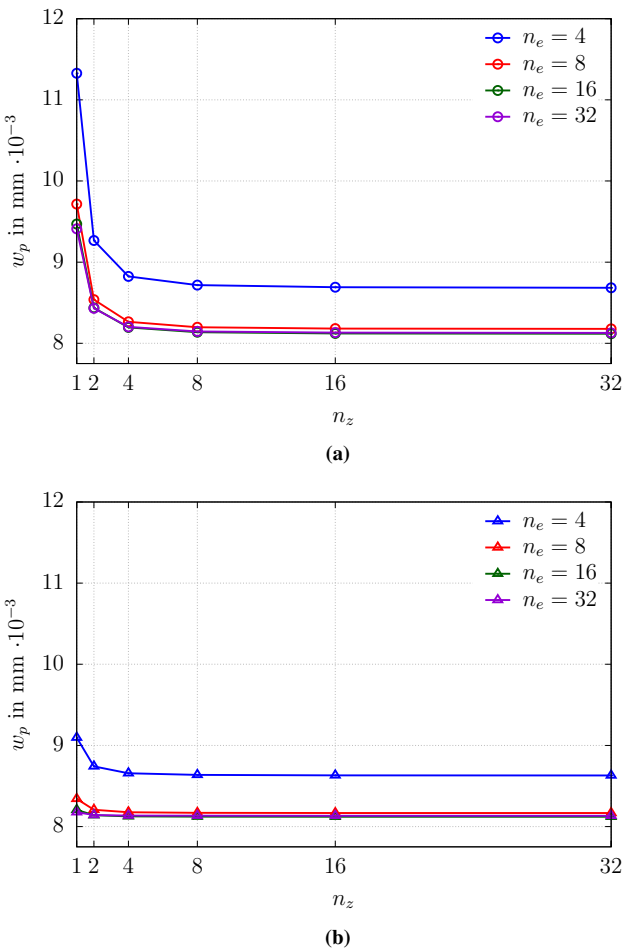

Fig. 19 Deflection w_P at the central point of the plate for different number of elements in planar and thickness directions ($a/h = 100$). **a** Q1SP element formulation, **b** Q1STs element formulation with 3 integration points in thickness direction

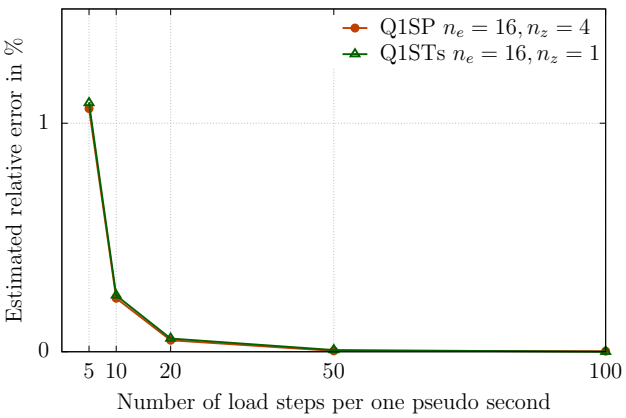

Fig. 20 Estimated relative error of the point P with $a/h = 100$ against different number of load steps in one pseudo second

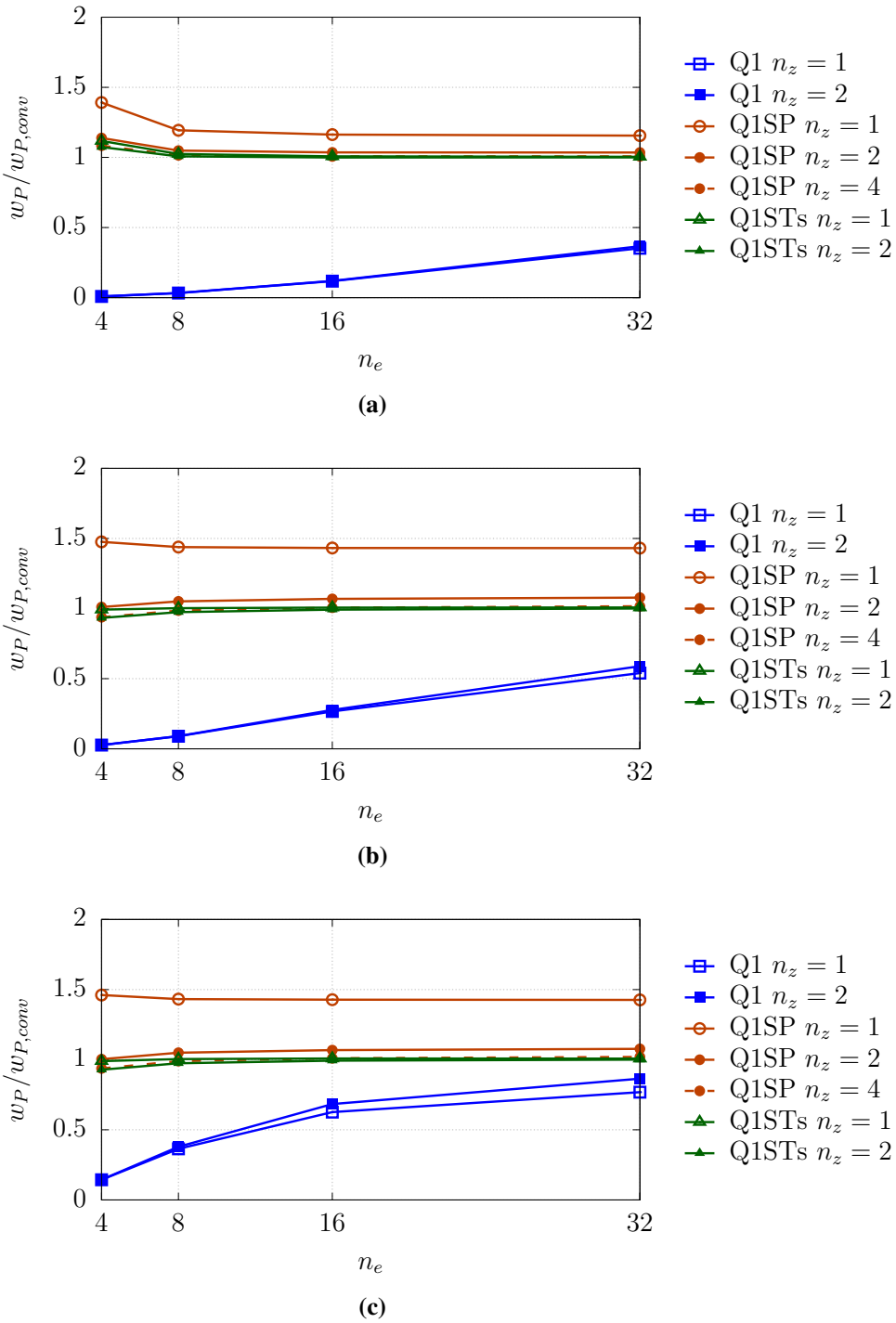

Fig. 21 Deflection at the central point of the thick plate for different number of elements (n_e) in planar directions. **a** $a/h = 100$, **b** $a/h = 50$ and **c** $a/h = 20$

The hourglass stabilization can be chosen constant. In this way, the deformation of the element is not considered. Another option is to take the deformation of the element into account and change the hourglass stabilization based on the deformed element configuration. To maintain quadratic convergence in the Newton iterations, the stabilization must be kept constant within the load step. This action could bring about a dependency of the solution on the number of load steps (Reese et al. [32]). To examine this dependency, the convergence behavior of two element formulations with respect to the number of the load steps within a pseudo time range (1 sec) of a calculation is plotted in Fig. 20. The sensitivity of the results to the size of the load step is negligible as the estimated relative error ($|(w_p - w_{P,conv})/w_{P,conv}| \times 100$) lies around 1% for having only five load steps. Nonetheless, both element formulations converge quadratically in each load step as expected.

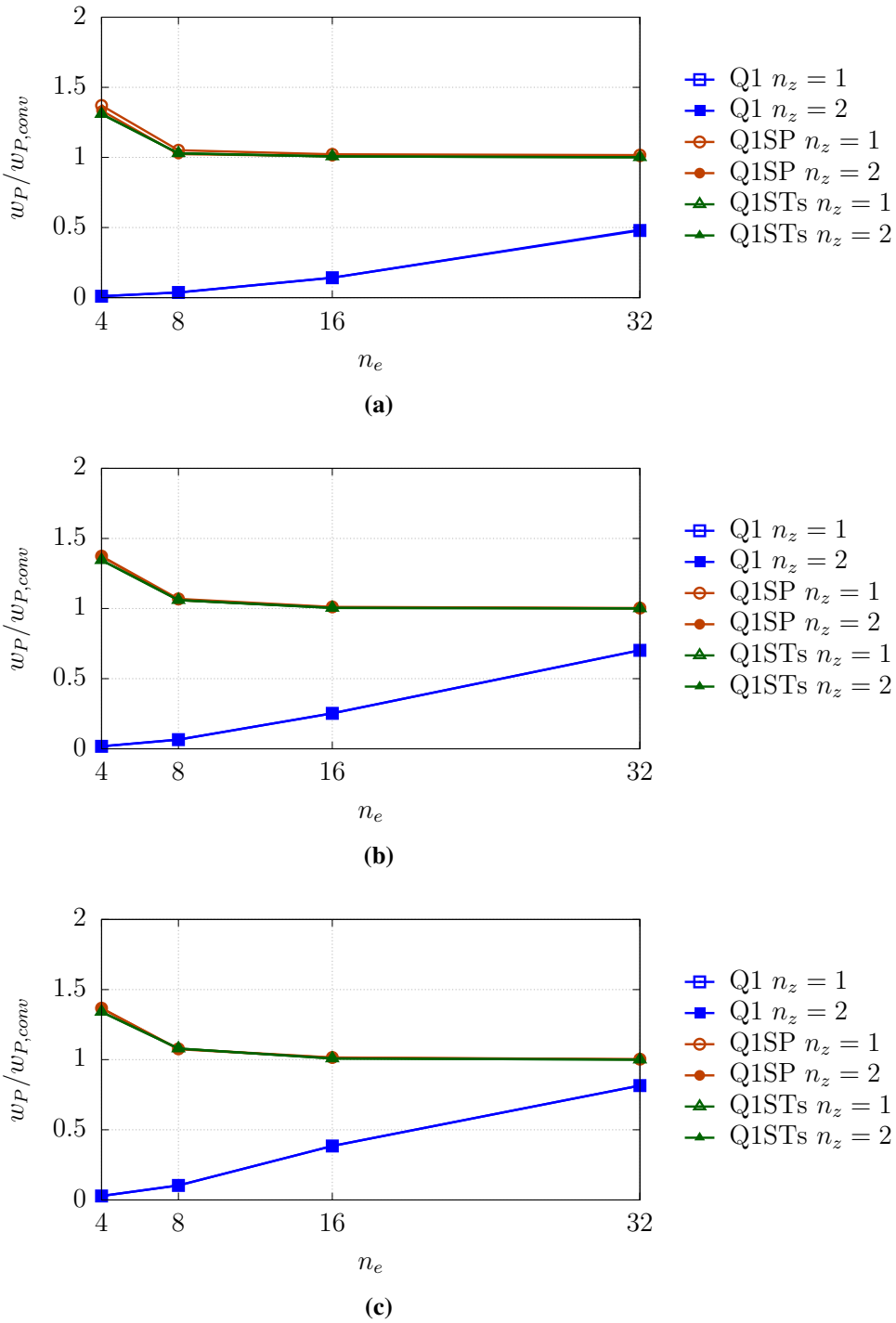

Fig. 22 Deflection at the central point of the thin plate for different number of elements (n_e) in planar directions. **a** $a/h = 200$, **b** $a/h = 500$ and **c** $a/h = 1000$

4.4.2 Influence of the Geometrical Aspect Ratio

The relative displacement $w_P/w_{P,conv}$ at the point P with respect to the converged solution $w_{P,conv}$ is investigated for thick as well as thin plates in Figs. 21 and 22, respectively. The x-axis of theses figures describes the mesh refinement in the planar directions as follows: $4 \times 4, 8 \times 8, 16 \times 16$ and 32×32, indicating the number of elements in x and y-direction, respectively.

Figure 21 pictures the behavior of different element formulations for thick plates. In our examples, this implies the geometrical aspect ratio $a/h \geq 50$ with $a/h = 100$ lying between the thick and thin plate regimes. The Q1STs element formulation overcomes the problem of transverse shear locking with very few number of elements (almost one) in

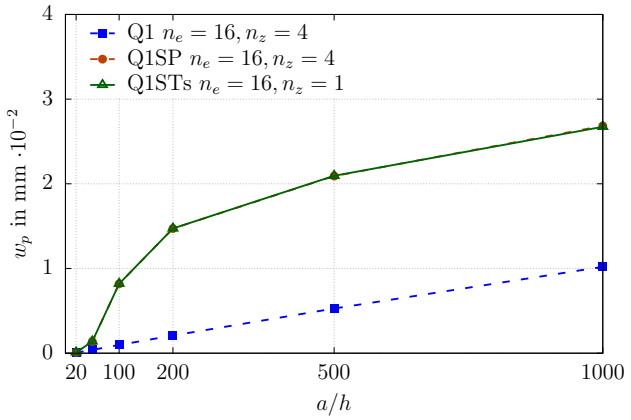

Fig. 23 Vertical displacement w_P at the point P with different thicknesses h

z-direction due to the application of assumed natural strain (ANS) concept. On the other hand, The Q1SP element needs more elements in the thickness direction to correctly capture the shear deformations. Only few number of elements in the planar directions are used for these two elements since these elements eliminate shear locking effects. On the contrary, the Q1 element observes severe locking due to the presence of shear locking in spite of the refinement of the mesh.

For much thinner structures (here, $a/h \leq 200$ illustrated in Fig. 22), the transverse shear deformations become negligible and thus transverse shear locking effects tend to disappear. In other words, for too high aspect ratios ($a/h = 1000$), the shell becomes a membrane in our example. This means that the need for the ANS concept in the solid-shell element formulation becomes less pronounced. As a result, both solid (Q1SP) and solid-shell (Q1STs) element formulations tend to perform similarly. Unlike the outstanding convergence rate of these two element formulations, the Q1 element shows still severe shear locking effects. However, by making the structures excessively thinner, the convergence rate of the Q1 element shows a slight increase. This can be due to the fact that by changing the geometries from shell to membrane, the bending stresses start to decrease.

Finally, the vertical displacement w_P at the point P is plotted for different geometrical aspect ratios in Fig. 23. The size of the mesh is set to the coarsest level which is necessary for the Q1SP and Q1STs element formulations to converge. For these mesh refinement levels, the Q1 elements show severe locking effects.

5 Material Interfaces

This collection of benchmarks pose the challenge of resolving material interfaces as well as high gradients or singularities induced by them. Especially discretization methods that avoid geometry conforming meshes, as presented e.g. in [33–35] will find interesting challenges in the presented two-dimensional benchmarks. Some extensions towards three dimensions can be found in [36].

In the following benchmarks, the convergence is measured by the relative error in the total energy with respect to the reference solution

$$\|e\|_{\mathcal{U}} = \sqrt{\frac{|\mathcal{U}_{\text{ex}} - \mathcal{U}|}{\mathcal{U}_{\text{ex}}}} \times 100\%, \tag{5.1}$$

where $\mathcal{U}_{\text{ex}}$ and $\mathcal{U}$ denote the exact and approximated energy, respectively. For a linear elastic problem $\mathcal{U} = \frac{1}{2}\int_\Omega \boldsymbol{\sigma} : \boldsymbol{\varepsilon} \mathrm{d}\Omega$ and for a heat conduction problem $\mathcal{U} = \frac{1}{2}\int_\Omega \kappa \nabla u \cdot \nabla u \mathrm{d}\Omega$.

Two types of discretization methods, Isogeometric Analysis (IGA) [37] and p-FEM [38], are used to provide reference solutions for the energy $\mathcal{U}_{\text{ex}}$ on locally refined conforming meshes. Curved geometries are represented in IGA using NURBS or B-splines while the blending function method [38] is used in the p-version of the finite element method. The unknown field variable is approximated in IGA using

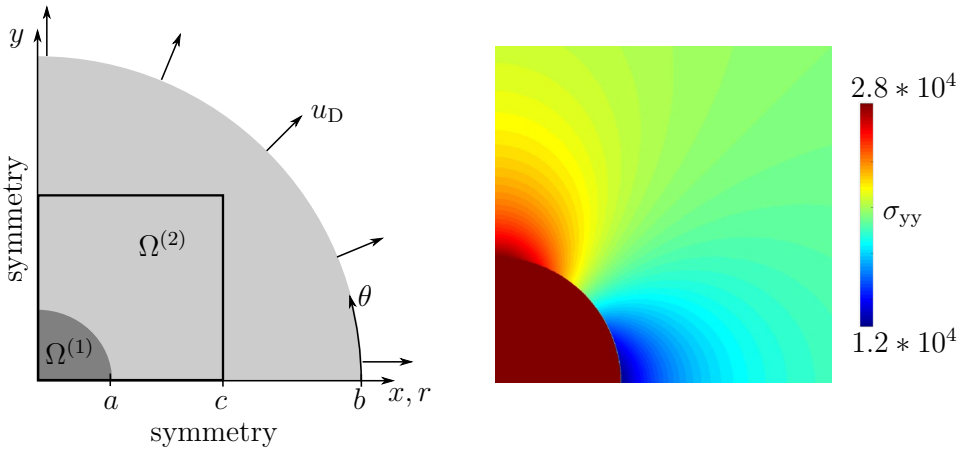

Fig. 24 Circular inclusion problem: model problem with domain and boundary condition as well as stress solution for σ_{yy} is illustrated in marked part of the domain

Table 20 Circular inclusion problem: dimensions of the domain in Fig. 24

a	b	c
3	15	8

Table 21 Circular inclusion problem: material parameters

$E^{(1)}$	$\nu^{(1)}$	$E^{(2)}$	$\nu^{(2)}$
1×10^4	0.3	1×10^5	0.3

Bézier extraction of truncated hierarchical B-splines [39] in combination with a safe refinement strategy [40]. In p-FEM geometrically graded meshes are used. In those cases where no analytic solution is available, improved energy values are obtained by the extrapolation technique described in [38].

In the following, all material and geometric parameters are given in consistent units.

5.1 Circular Inclusion

This benchmark is to test the representation of stress and strain fields across a material interface. The solution on the rest of the domain is smooth and optimal convergence rates should be achieved easily once the discontinuity introduced by the material interface is resolved properly. An analytical solution is available.

5.1.1 System

The two-dimensional plane strain problem is governed by the partial differential equations of linear elastostatics without body load. Given in the strong form of the boundary value problem it reads:

$$\nabla \cdot \boldsymbol{\sigma}^{(i)} = \mathbf{0} \quad \forall \boldsymbol{x} \in \Omega^{(i)}, \quad i = 1, \dots, n, \tag{5.2a}$$

$$\boldsymbol{\sigma}^{(i)} = \mathbb{C}^{(i)} : \boldsymbol{\varepsilon}(\boldsymbol{u}^{(i)}) \quad \forall \boldsymbol{x} \in \Omega^{(i)}, \quad i = 1, \dots, n, \tag{5.2b}$$

$$\boldsymbol{\varepsilon}(\boldsymbol{u}^{(i)}) = \frac{1}{2}\left(\nabla \boldsymbol{u}^{(i)} + \nabla \boldsymbol{u}^{(i)^{\mathsf{T}}}\right) \quad \forall \boldsymbol{x} \in \Omega^{(i)}, \quad i = 1, \dots, n, \tag{5.2c}$$

where $\Omega^{(1)}, \Omega^{(2)} \subset \mathbb{R}^2$ are defined in Fig. 24, $\boldsymbol{\sigma}^{(i)}$ is the stress tensor, $\mathbb{C}^{(i)}$ the plane strain elastic material tensor, $\boldsymbol{\varepsilon}$ the strain tensor, and $\boldsymbol{u}^{(i)}$ is the displacement vector of the sub-domain $\Omega^{(i)}$. The circular inclusion $\Omega^{(1)}$ has material parameters E_1, ν_1 and a radius a that is embedded in an isotropic and linear elastic (E_2, ν_2) disc $\Omega^{(2)}$ with radius b. A radial displacement is applied on the outer boundary as depicted in Fig. 24. The problem can be solved analytically under plane strain conditions leading to the displacement field in polar coordinates [41]

$$u_r = \begin{cases} \left[\left(1 - \frac{b^2}{a^2}\right)\alpha + \frac{b^2}{a^2}\right] r & \text{for } 0 \le r \le a \\ \left(r - \frac{b^2}{r}\right)\alpha + \frac{b^2}{r} & \text{for } a \le r \le b \end{cases} \tag{5.3}$$

$$u_\theta = 0 \tag{5.4}$$

with

$$\alpha = \frac{(\lambda_1 + \mu_1 + \mu_2)b^2}{(\lambda_2 + \mu_2)a^2 + (\lambda_1 + \mu_1)(b^2 - a^2) + \mu_2 b^2} \tag{5.5}$$

and the Lamé parameters λ and μ. The strains are given by $\epsilon_r = u_{r,r}$ and $\epsilon_\theta = \frac{u_r}{r}$ and the stresses by $\sigma_r = 2\mu\epsilon_r + \lambda(\epsilon_r + \epsilon_\theta)$ and $\sigma_\theta = 2\mu\epsilon_\theta + \lambda(\epsilon_r + \epsilon_\theta)$.

To reduce the computational effort, the problem is only solved on a square with dimension c cut out of the cylinder. This setting eases the application of boundary conditions and thereby avoids additional error sources, especially if embedded domain methods with a regular background mesh are used. Homogeneous Dirichlet boundary conditions are applied at the lower and left edge of the square in y and x direction, respectively. Neumann boundary conditions are

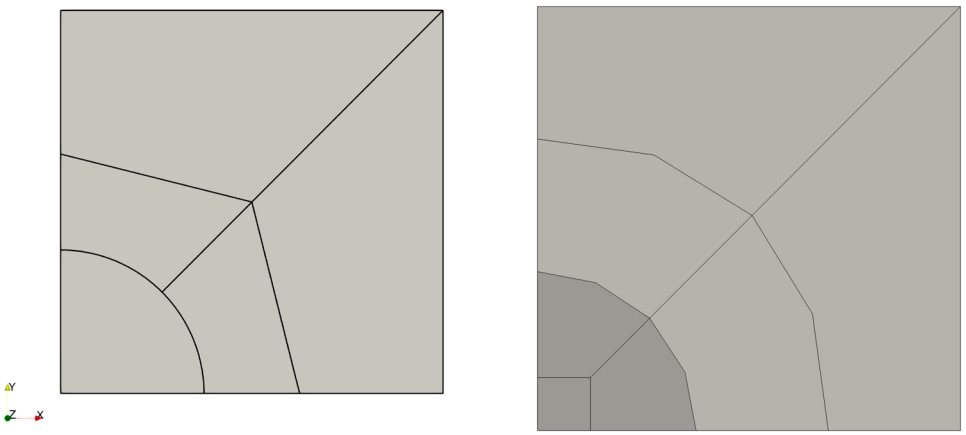

Fig. 25 Circular inclusion problem: initial mesh for p-FEM (left) and IGA (right) discretization are illustrated. Please note that the NURBS mesh represents the circle exactly. Linear approximation results from post processing only

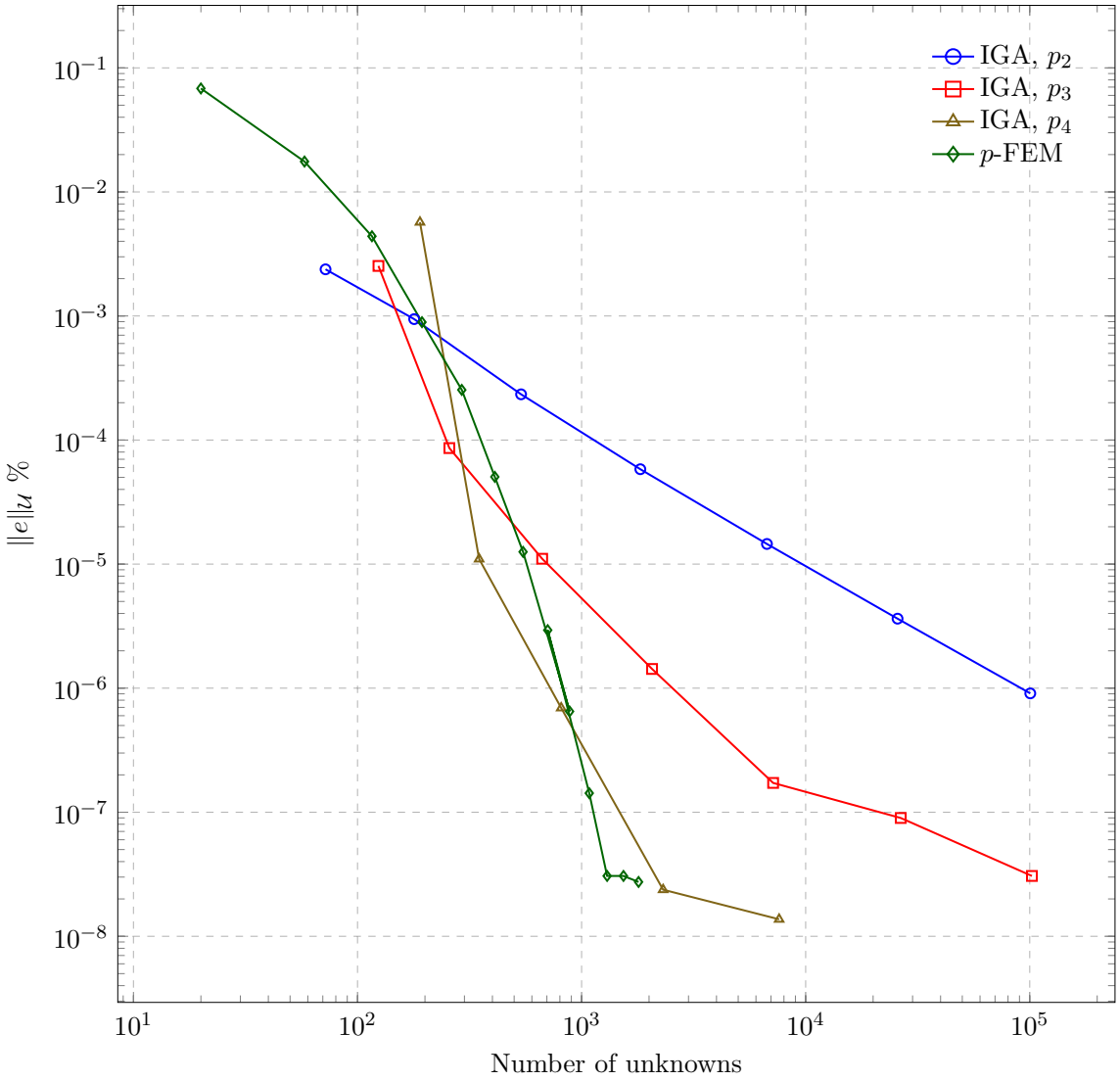

Fig. 26 Circular inclusion problem: convergence of total energy

Table 22 Circular inclusion problem: the strain energy $\mathcal{U}$ and corresponding degrees of freedom DOF are given for the p-FEM and IGA ($p = 4$) computation

p-FEM		IGA, p_4	
DOF	$\mathcal{U}/10^6$	DOF	$\mathcal{U}/10^6$
20	1.234078137645319	201	1.239852423077503
194	1.239851448235106	379	1.239852433716069
884	1.239852433865278	903	1.239852433865204
1796	1.239852433865801	2623	1.239852433865802

applied at the upper and right edge of the square using the analytical stresses.

The dimensions are given in Table 20 and the material parameters in Table 21. The analytically computed strain energy is

$$\mathcal{U}_{\text{ex}} = 1.239852433865801 \times 10^6.$$

5.1.2 Discretization and Results

An overall impression of the stress state σ_{yy} is provided in Fig. 24. The jump of the stresses at the material interface is clearly visible.

The p-FEM discretization uses 5 elements. The circular shape at their boundary is represented exactly using the blending function method, c.f. Fig. 25. The solution is obtained by keeping the element mesh fixed and uniformly

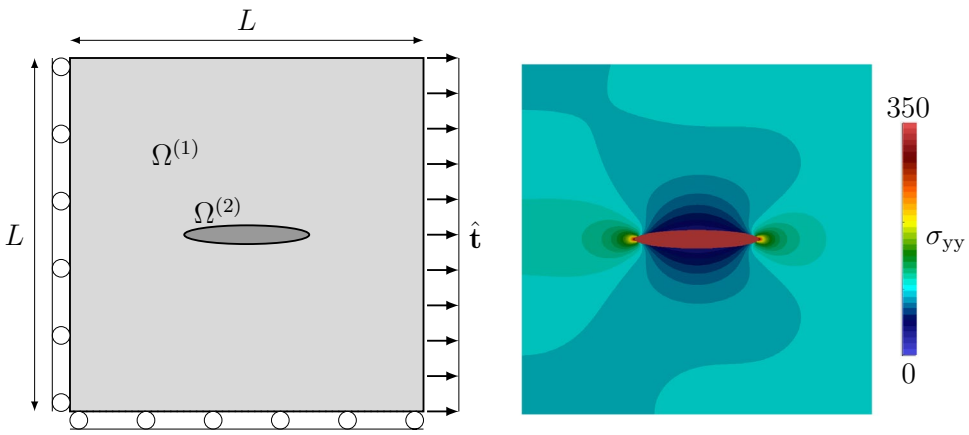

Fig. 27 Elliptical inclusion problem: model problem with domain and boundary condition as well as stress solution for σ_{yy} is illustrated

Table 23 Elliptical inclusion problem: dimensions of the domain

L	r_x	r_y
2	$\sqrt{0.125}$	$0.15r_x$

Table 24 Elliptical inclusion problem: material parameters and traction load

$E^{(1)}$	$\nu^{(1)}$	$E^{(2)}$	$\nu^{(2)}$	$\lvert\hat{t}\rvert$
210×10^3	0.3	210×10^4	0.3	100

increasing the polynomial degree of the basis functions of each element (uniform p-refinement).

The IGA discretization is based on 7 NURBS-patches using at least a bi-quadratic basis that allows for an exact geometric representation of the circular inclusion, c.f. Fig. 25. The basis is C^0-continuous along the material interface. Due to the absence of singularities and the mild stress concentration, an uniform mesh refinement under constant polynomial degrees was carried out in the convergence studies.

The results of the convergence study are shown in Table 22 and illustrated in Fig. 26. It is clearly visible that due to the C^0-continuous basis along the material interface and the absence of singularities, all methods are able to reproduce optimal convergence rates. For both methods, p-FEM and IGA with $p = 4$, only 1000 degrees of freedom are needed to compute a strain energy that equals the analytically computed strain energy except for the last digit.

5.2 Elliptical Inclusion

The second benchmark is a linear elastic plane stress problem of an embedded elliptical inclusion. The high aspect ratio of the ellipse leads stress concentrations that have to be resolved.

5.2.1 System

The model problem is again defined by Eq. (5.2), where $\mathbb{C}^{(i)}$ is the plane stress material tensor, $\Omega^{(2)}$ is an elliptical inclusion with material parameters E_1, ν_1 and aspect ratio r_y/r_x that is embedded into a quadratic plate $\Omega^{(1)}$ with material parameters E_2, ν_2 and dimension L. The domain and boundary conditions are given in Fig. 27. The dimensions and material properties are depicted in Tables 23 and 24,

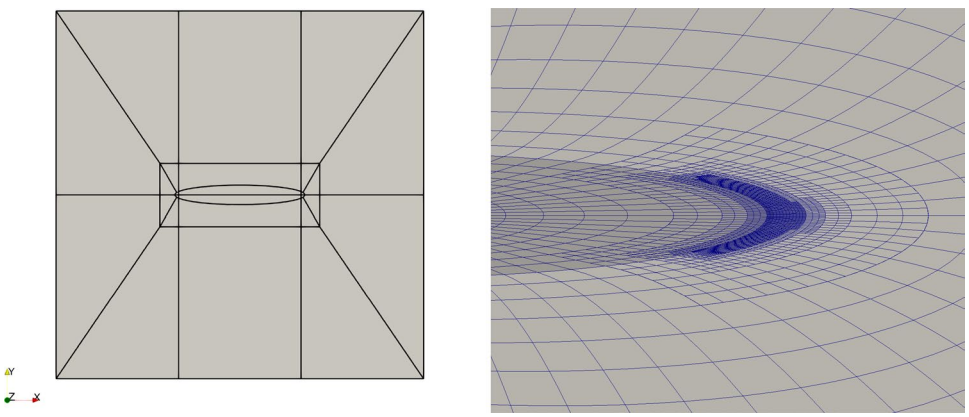

Fig. 28 Elliptical inclusion problem: initial mesh for P-FEM (left) and locally refined mesh for IGA (right) discretization are illustrated. In IGA the mesh is refined towards the stress concentration at the material interface

Table 25 Elliptical inclusion problem: the strain energy $\mathcal{U}$ and corresponding degrees of freedom DOF are given for the p-FEM and IGA ($p = 6$) computation

p-FEM		IGA, p_6	
DOF	$\mathcal{U}/10^{-2}$	DOF	$\mathcal{U}/10^{-2}$
1934	9.1012391771635864	4785	9.101254710960735017
5302	9.1013093250777097	5323	9.101304183498346023
10,334	9.1013110991904414	6553	9.101310846723154046
17,030	9.1013111641365024	9347	9.101311158196075112
25,390	9.1013111663629354	22,059	9.101311166401243602
35,414	9.1013111664396851	59,127	9.101311166441683475

respectively. The disc has a loose bearing on the lower and left side and a traction load $\hat{\boldsymbol{t}}$ is applied to the right side of the disc.

5.2.2 Discretization and Results

To validate the extrapolated reference energy, the convergence of the solution is measured in the energy norm for p-refinement in a FE analysis and for h-refinement in an isogeometric analysis.

In the case of IGA, 12 patches are used to discretise the computational domain. The elliptical shape of the material interface is represented exactly using NURBS. To properly resolve the stress concentration, the mesh is refined using Bézier extraction of truncated hierarchical B-splines [39] as

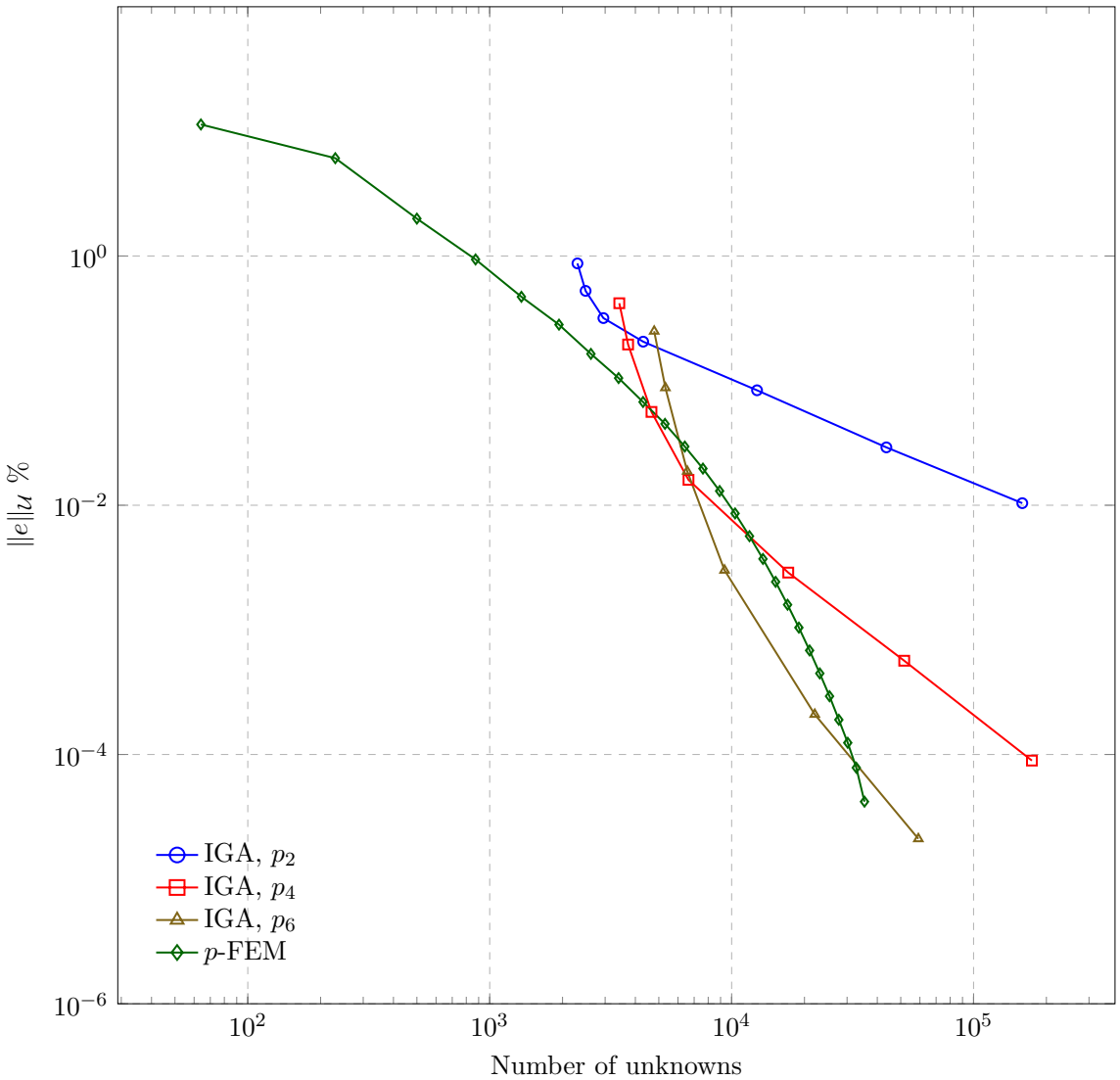

Fig. 29 Elliptical inclusion problem: convergence in energy norm

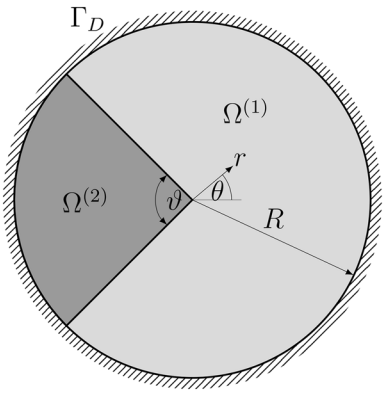

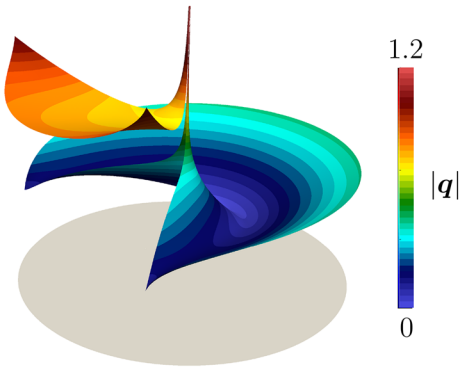

Fig. 30 Inclusion with a corner: model problem with domain and boundary condition as well as heat flux magnitude is illustrated

Table 26 Inclusion with a corner: dimensions of the domain in Fig. 30

R	ϑ
1	$\pi/2$

Table 27 Inclusion with a corner: material parameters and traction load

$k^{(1)}$	$k^{(2)}$
1	10

illustrated in Fig. 28 on the right. To allow for well graded meshes, a safe refinement strategy is used [40]. Starting from an initial mesh of 768 elements, seven refinement steps are performed for three different polynomial degrees. To also refine the vicinity of the stress concentration, the maximum number of hierarchical levels in a computation is restricted to four.

In the case of p-FEM, the domain is discretized by a mesh composed of 26 elements with blended edges conforming to the material interface. The mesh is spatially graded towards the stress concentration due to the high curvature of the interface at the major axis of the ellipse. The solution σ_{yy} and the graded meshes are depicted in Figs. 27, and 28. To obtain a reference solution, the energy computed for a discretization with polynomial degrees $p = 30$ and $p = 47$ is extrapolated. The extrapolated value is

$$\mathcal{U}_{\text{ex}} = 9.10131116644128 \times 10^{-2}.$$

As shown in Table 25 and illustrated in Fig. 29, both discretization methods converge to the extrapolated reference energy.

5.3 Inclusion with a Corner

The third benchmark is a linear Poisson problem with a sharp inclusion adapted from [42]. The re-entrant corner at the material interface leads to a singularity in the solution.

5.3.1 System

This benchmark is governed by the Poisson equation:

$$\kappa^{(i)} \nabla^2 \phi^{(i)} = -1 \quad \forall \boldsymbol{x} \in \Omega^{(i)} \tag{5.6}$$

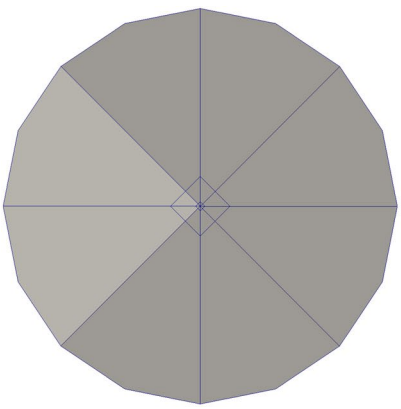

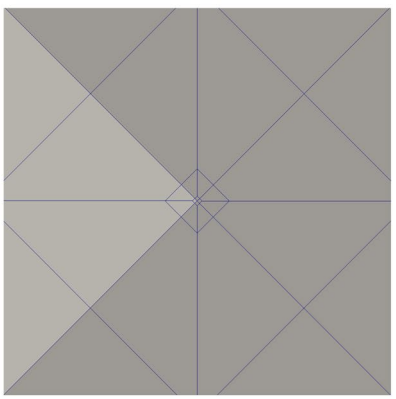

Fig. 31 Inclusion with a corner: the initial mesh for IGA (left) consists of 28 patches and is locally refined towards the singularity (zoom on the right). The NURBS mesh represents the outer circle exactly. The visible linear approximation results from post processing only

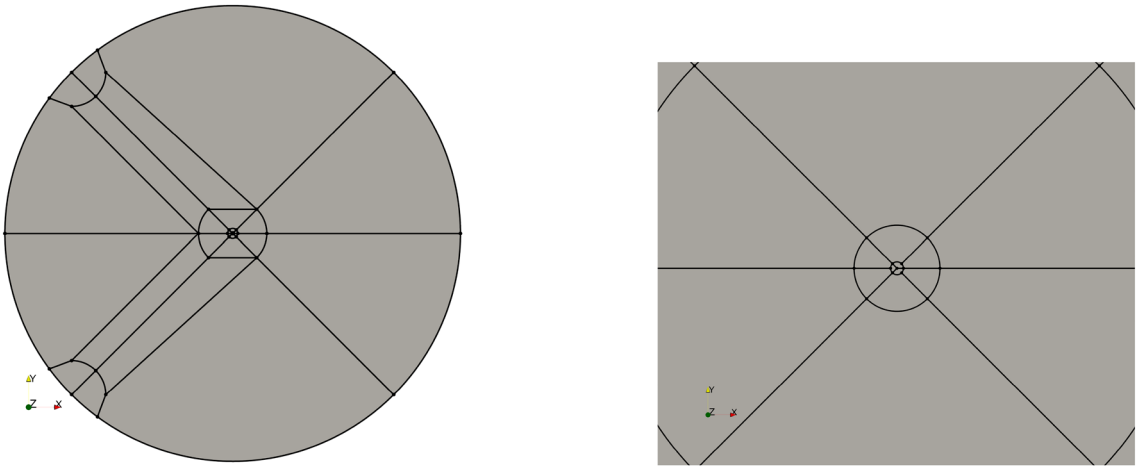

Fig. 32 Inclusion with a corner: the initial mesh for p-FEM (left) is locally refined towards the singularity (zoom on the right)

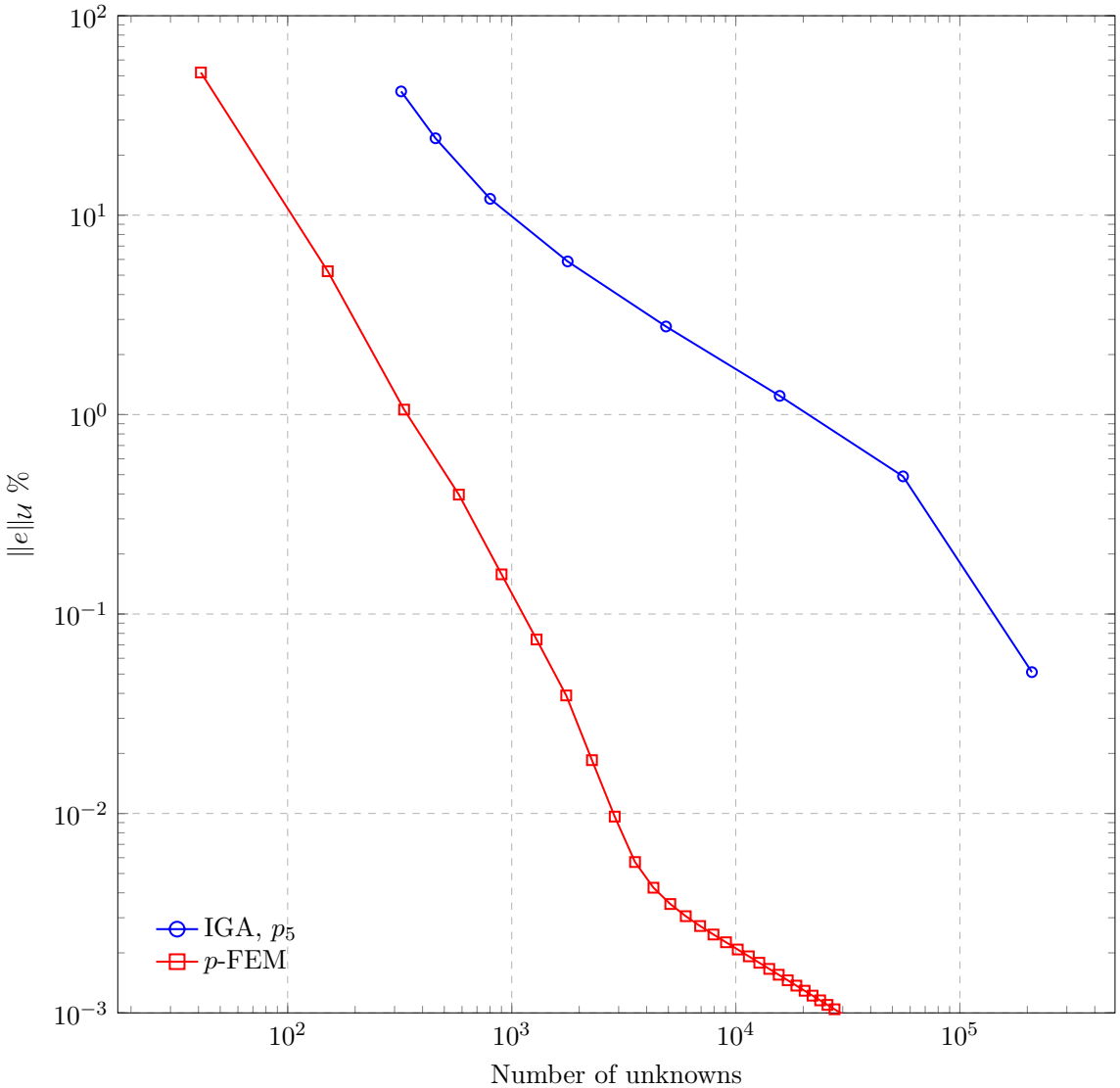

Fig. 33 Inclusion with a corner: convergence in energy norm

Table 28 Inclusion with a corner: the energy $\mathcal{U}$ and corresponding degrees of freedom DOF are given for the p-FEM and IGA ($p = 5$) computation

p-FEM		IGA, p_5	
DOF	$\mathcal{U}/10^{-1}$	DOF	$\mathcal{U}/10^{-1}$
41	0.74283160340255783	321	0.83969400295
581	1.0168282915873117	457	0.95680748948
2281	1.0168442811407008	801	1.00201905312
5101	1.0168443147188094	1777	1.01334969314
9041	1.0168443154555366	4881	1.01606662635
14,101	1.0168443156940091	15,697	1.01668762623
20,281	1.0168443158052781	55,761	1.01681988939
31,651	1.0168443158835522	209,617	1.01684404869

$$\phi = 0 \quad \forall \boldsymbol{x} \in \Gamma_D, \tag{5.7}$$

where $\phi^{(i)}$ denotes the temperature, $\kappa^{(i)}$ the thermal diffusivity, $\Omega^{(i)}$ and Γ_D are defined as shown in Fig. 30. The dimensions and material properties are given in Tables 26 and 27, respectively. Here, the material interface Γ_{12} has a sharp corner, inducing a vertex singularity. Moreover, the intersection of the material interface with the Dirichlet boundary Γ_D introduces two additional weak singularities where the solution exhibits reduced continuity.

The exact solution to this problem is given in polar coordinates (r, θ) by [43]:

$$\phi(r, \theta) = A_1 r^{\lambda_1} h_1(\theta) + A_2 r^{\lambda_2} h_2(\theta) + \mathcal{O}(r^2), \tag{5.8}$$

where A_1 and A_2 are scalar constants, $h_1(\theta)$ and $h_2(\theta)$ are smooth sinusoidal functions and

$$\lambda_1 = 0.731691779, \quad \lambda_2 = 1.268308221. \tag{5.9}$$

5.3.2 Discretization and Results

The domain is discretized by 28 NURBS patches with at least quadratic polynomial degree to exactly represent the circular outer boundary of the domain, see Fig. 31. The initial mesh is locally refined towards the singularity at the re-entrant corner. Due to the local pre-refinement, uniform refinement was applied in the convergence study of the IGA discretization.

The p-FEM discretization is depicted in Fig. 32. As in the previous examples, the mesh is conforming to material interface and the domain boundary is exactly represented by means of the blending function method. The mesh is graded geometrically towards the singularity located at the re-entrant corner, see Fig. 32. The problem is solved by keeping the mesh fixed and performing a uniform p-extension.

For this example, the extrapolated reference energy is given by

$$\mathcal{U}_{\text{ex}} = 1.016844315974886 \times 10^{-1}.$$

The convergence of the p-FEM and the IGA discretizations shown in Table 28 and illustrated in Fig. 33. In this case the grading of the p-FEM mesh towards the singularities considerably improves the accuracy per degree of freedom.

6 Phase Field Model for Brittle Fracture

6.1 Mathematical Model

Phase field models for fracture were introduced by the seminal works of Francfort and Marigo [44], Bourdin et al. [45], Bourdin [46]. Initially developed as a regularized version of the fracture mechanical treatment of cracks in the spirit of Griffith, recent extensions treat dynamic and inelastic fracture processes. In order to provide a robust setup for different numerical schemes and discretization methods, the proposed benchmarks are straightforward and disregard special problems concerning the distinction between tension and compression, as well as subtleties in the evolution equation. Details on these issues can for example be found in Kuhn [47].

With these preliminary remarks, we state the governing differential equations, which follow the original work of Bourdin [46]. Starting point is the free energy density of the system

$$\begin{aligned}\Psi(\boldsymbol{\varepsilon}, s) =& (s^2 + \eta) W(\boldsymbol{\varepsilon}) \\ &+ \mathcal{G}_c \left(\frac{1}{4\epsilon}(1 - s)^2 + \epsilon |\nabla s|^2 \right)\end{aligned} \tag{6.1}$$

which depends on the strain field $\boldsymbol{\varepsilon}$ and the fracture field s. The meaning of s is the following: If $s = 1$ the material is intact, while $s = 0$ represents the fully broken material. The parameters $\mathcal{G}_c$ and ϵ describe the cracking resistance (related to the fracture toughness) and the width of the regularization zone. The parameter η models the residual stiffness of the fully broken material ($s = 0$). The residual stiffness is required to ensure a non vanishing stiffness in a static analysis. In (6.1) $W(\boldsymbol{\varepsilon})$ represents the elastic strain energy density. If an isotropic material behavior is assumed the strain energy density can be expressed with the help of the two Lamé constants λ and μ by

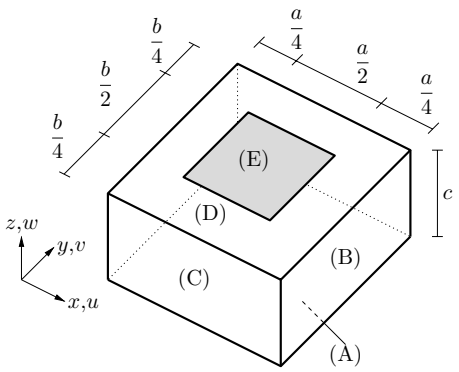

Fig. 34 Geometry of the 3D benchmark problem

$$W(\boldsymbol{\varepsilon}) = \frac{1}{2}\lambda(\mathrm{tr}\,\boldsymbol{\varepsilon})^2 + \mu\,\boldsymbol{\varepsilon} : \boldsymbol{\varepsilon} \quad \text{with}$$
$$\boldsymbol{\varepsilon} = \frac{1}{2}\left(\nabla\boldsymbol{u} + \nabla^{\mathrm{T}}\boldsymbol{u}\right) \tag{6.2}$$

where $\boldsymbol{\varepsilon}$ is the linearized strain, and $\boldsymbol{u}$ represents the displacement field. The " : " in (6.2) indicates the scalar product between two second order tensors, and "tr" is the trace of a second order tensor. The free energy density (6.1) defines the stress $\boldsymbol{\sigma}$ via

$$\boldsymbol{\sigma} = \frac{\partial\Psi}{\partial\boldsymbol{\varepsilon}} = (s^2 + \eta)(\lambda\,\mathrm{tr}\,\boldsymbol{\varepsilon}\,\mathbf{1} + 2\mu\,\boldsymbol{\varepsilon}) \tag{6.3}$$

where $\mathbf{1}$ is the second order identity tensor. The stress has to satisfy the equilibrium condition

$$\mathrm{div}\boldsymbol{\sigma} = \mathbf{0}, \tag{6.4}$$

with "div" as the divergence. Thus volume forces are neglected. The static mechanical problem has to be supplied with proper boundary conditions, either Dirichlet conditions

$$\boldsymbol{u} = \boldsymbol{u}^* \quad \text{on}\ \partial\mathcal{B}_u \tag{6.5}$$

with prescribed displacements $\boldsymbol{u}^*$ on the displacement boundary $\mathcal{B}_u$, or Neumann conditions

$$\boldsymbol{\sigma}\boldsymbol{n} = \boldsymbol{t}^* \quad \text{on}\ \partial\mathcal{B}_\sigma \tag{6.6}$$

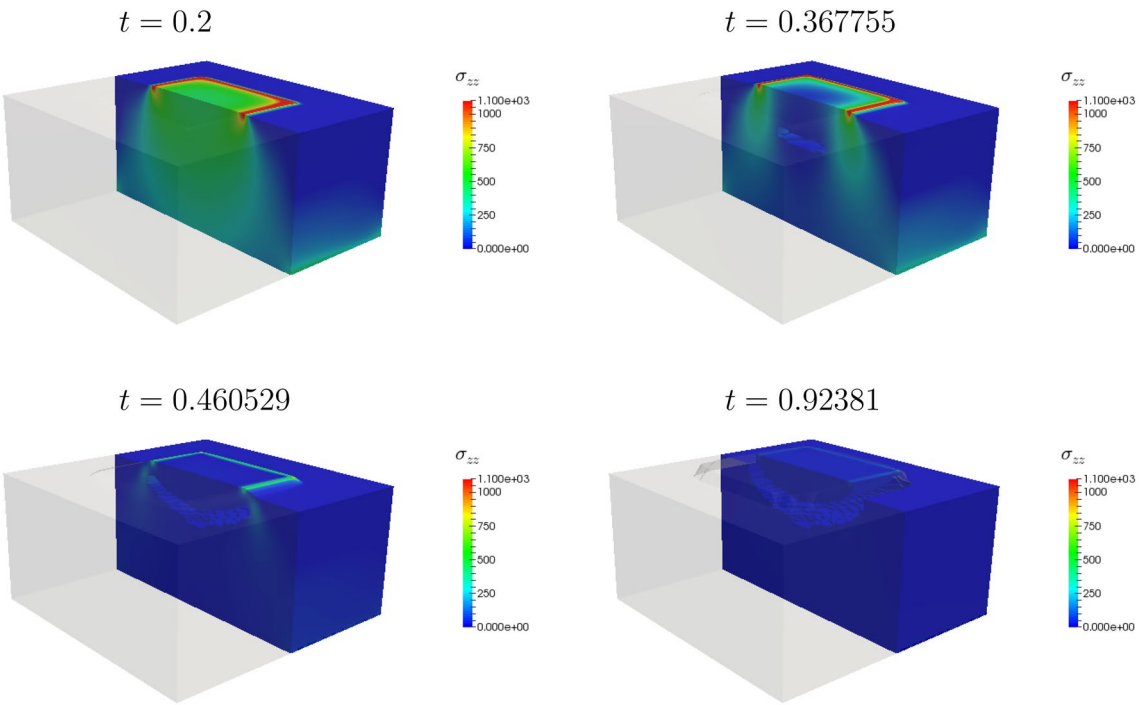

Fig. 35 Evolution of crack configuration and normal stress σ_{zz} at four time steps ($t = 0.2/0.367755/0.460529/0.92381$). Elements with $s < 0.05$ are suppressed in the plots to indicate fracture

Table 29 Number of degrees of freedom for different spatial discretisations

n	10	20	30	40	50	60
d.o.f.	4861	35,237	115,381	268,877	520,301	892,917

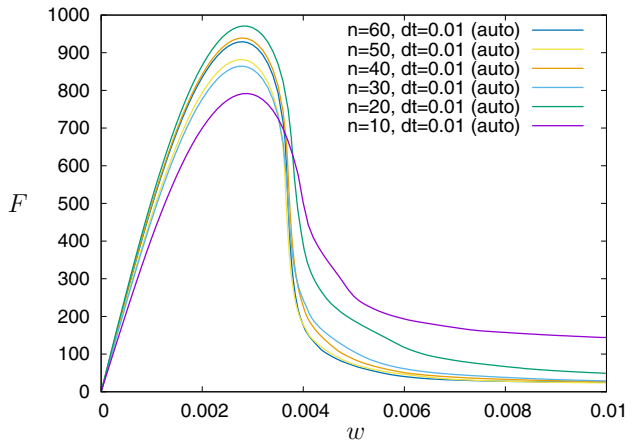

Fig. 36 Displacement-reaction force curve for different spatial discretisations

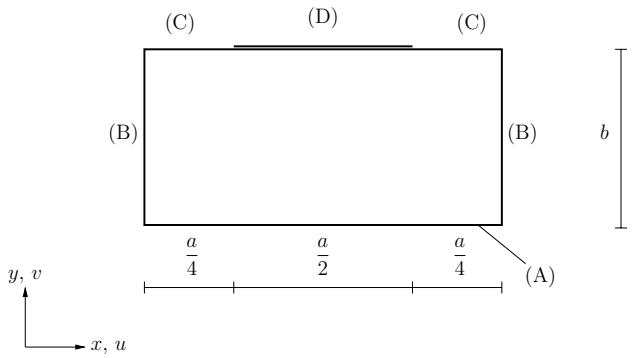

Fig. 37 Geometry of the 2D benchmark problem

with prescribed traction $\boldsymbol{t}^*$ on the traction boundary $\mathcal{B}_\sigma$. The vector $\boldsymbol{n}$ denotes the outward unit normal. The fracture field s is governed by an nonlocal evolution equation, which is driven by the variational derivative of the free energy with respect to s. In the terminology of phase field models this evolution equation is also referred to as the time dependent Ginzburg-Landau equation:

$$\begin{aligned}\dot{s} &= -M\,\frac{\delta\Psi}{\delta s}\\ &= M\left[2\mathcal{G}_c\epsilon\,\Delta s - 2s\,W(\boldsymbol{\varepsilon}) + \frac{\mathcal{G}_c}{2\epsilon}(1-s)\right],\end{aligned} \tag{6.7}$$

where $\dot{s}$ is the rate of s with respect to time t, and "Δ" denotes the Laplace operator. The mobility constant M has to chosen sufficiently large to approximate quasi-static crack growth conditions. The fracture field is also associated with either Dirichlet conditions

$$s = s^* \quad \text{on } \partial\mathcal{B}_s \tag{6.8}$$

with prescribed fracture field s^* on the Dirichlet boundary $\mathcal{B}_s$, or Neumann conditions

$$\partial s_n = \nabla s \cdot \boldsymbol{n} = q^* \quad \text{on } \partial\mathcal{B}_q \tag{6.9}$$

with prescribed flux q^* on the flux boundary $\partial\mathcal{B}_q$. Frequently, homogeneous Neumann boundary conditions are set on the fracture field s and s is set to zero at certain locations to model initial cracks. Additionally, the fracture field $s(\boldsymbol{x}, t)$ has to be supplied by initial conditions, as (6.7) is a first order differential equation in time t. Thus, we must provide:

$$s(\boldsymbol{x}, 0) = s_0(\boldsymbol{x}). \tag{6.10}$$

If the material is unbroken and no preexisting cracks are treated, $s_0(\boldsymbol{x}) = 1$ everywhere.

To conclude the presentation of the mathematical model some remarks are given:

- the fracture field s is bounded $s \in [0, 1]$
- different evolution strategies are possible, see Kuhn [47]
  - damage-like behavior: $\dot{s} \leq 0$
  - indicator-like behavior: $\dot{s} = 0$ if $s = 0$
- different solution strategies are possible
  - monolithic solution of (6.4) and (6.7)
  - staggered solution of (6.4) and (6.7)

  using the stress from (6.3) and strain energy density from (6.2) in both strategies.

6.2 3D Setup

In Fig. 34a 3D initial-boundary value problem is defined on a block-like geometry. The block is loaded on a part of its top surface by a linearly increasing displacement load, while being fixed on the lower surface.

The following dimensionless parameters are used:

Geometry parameters:

$$a = 2, b = 2, c = 1 \tag{6.11}$$

Material and model parameters:

$$\begin{aligned}&\lambda = 100000, \mu = 100000, \epsilon = 0.1,\\ &\eta = 0.0001, \mathcal{G}_c = 1, M = 10\end{aligned} \tag{6.12}$$

Initial conditions at $t = 0$:

$$s_0 = 1 \tag{6.13}$$

Boundary conditions on the surfaces (A)-(E):

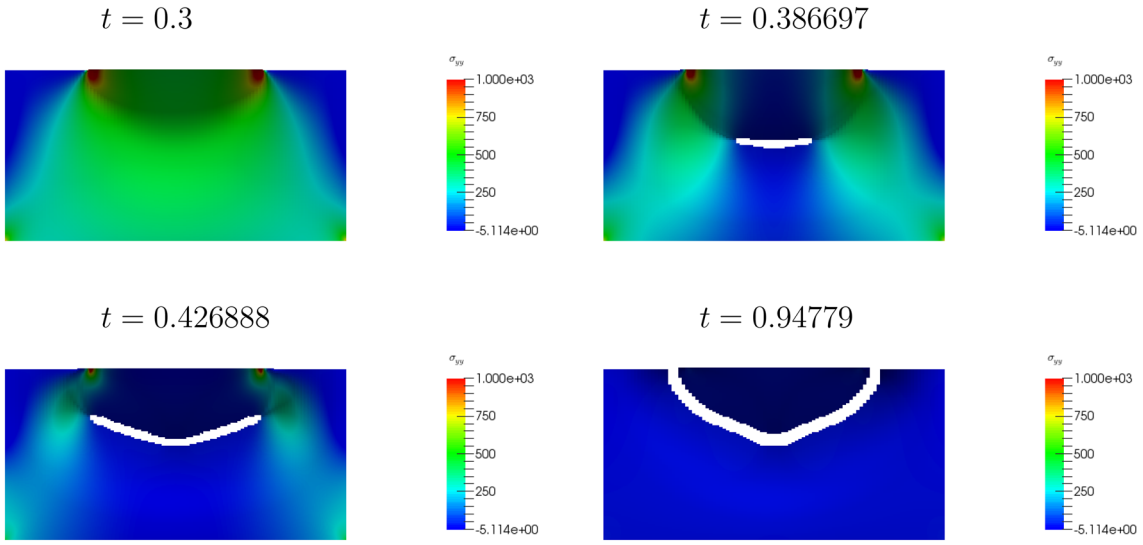

Fig. 38 Evolution of crack configuration and normal stress σ_{zz} at four time steps ($t = 0.3/0.386697/0.426888/0.94779$). Elements with $s < 0.05$ are suppressed in the plots to indicate fracture

Table 30 Number of degrees of freedom for different plane discretizartions

n	25	50	75	100	125	150
d.o.f.	1940	7626	17,061	30,248	47,190	67,876

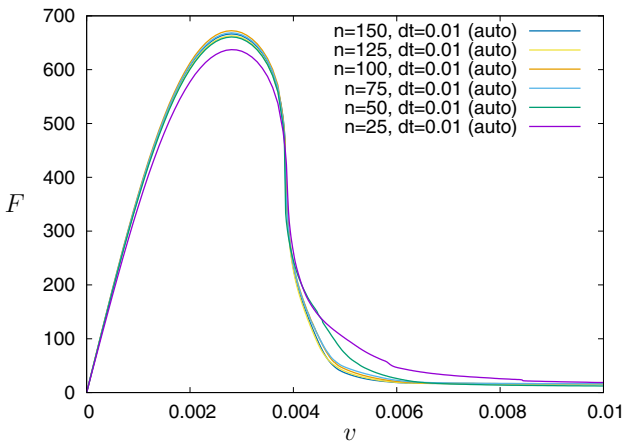

Fig. 39 Displacement-reaction force curve for different plane discretizations

$$
\begin{aligned}
&\text{(A)}: u = 0, v = 0, w = 0, && \partial_n s = 0\\
&\text{(B)}: \sigma_{xx} = 0, \sigma_{xy} = 0, \sigma_{xz} = 0, && \partial_n s = 0\\
&\text{(C)}: \sigma_{yy} = 0, \sigma_{xy} = 0, \sigma_{yz} = 0, && \partial_n s = 0\\
&\text{(D)}: \sigma_{zz} = 0, \sigma_{xz} = 0, \sigma_{yz} = 0, && \partial_n s = 0\\
&\text{(E)}: u = 0, v = 0, w = 0.01t, && s = 1
\end{aligned}
\tag{6.14}
$$

This setup leads to a crack initiation in the bulk. The crack then propagates to the top surface resulting in a shell like fracture surface. Intermediate steps of the computation are reported in Fig. 35. The finest mesh of Table 29 is used for the plots in Fig. 35.

The results are obtained by standard 8-node finite elements with tri-linear shape functions. The same spatial interpolation is used for u, v, w and s. The time integration of (6.7) is done by an implicit/backward Euler scheme using adaptive time step control. The initial time step is set to $\Delta t = 0.01$. The time step Δt is halved if the Newton method for the increments does not converge in 8 iterations. This time step halving is repeated at most 10 times. The time step Δt is increased to twice its value if 4 or less Newton iterations are required. Using n elements along the edges a, b and c, the number of degrees of freedom (d.o.f.) is reported in Table 29. The monolithic solution strategy was used. As a quantitative result, the reaction force F in z-direction on the segment (E)

$$
F = \int_{A(\mathrm{E})} \sigma_{zz} \, \mathrm{d}A \tag{6.15}
$$

is reported with respect to the prescribed displacement w in Fig. 36.

6.3 2D Setup

In Fig. 37 a 2D initial-boundary value problem is defined on a block geometry. The block is loaded on a half of its top

surface by a linearly increasing displacement load, while being fixed on the lower surface.

The following dimensionless parameters are used:

Geometry parameters:

$$a = 2, b = 1 \tag{6.16}$$

Material and model parameters:

$$\begin{aligned} &\lambda = 100000, \mu = 100000, \epsilon = 0.1, \\ &\eta = 0.0001, \mathcal{G}_c = 1, M = 10 \end{aligned} \tag{6.17}$$

Initial conditions at $t = 0$:

$$s_0 = 1 \tag{6.18}$$

Boundary conditions on the surfaces (A)-(D):

$$\begin{aligned} &\text{(A)} : u = 0, v = 0, \quad \partial_n s = 0 \\ &\text{(B)} : \sigma_{xx} = 0, \sigma_{xy} = 0, \partial_n s = 0 \\ &\text{(C)} : \sigma_{yy} = 0, \sigma_{xy} = 0, \partial_n s = 0 \\ &\text{(D)} : u = 0, v = 0.01t, s = 1 \end{aligned} \tag{6.19}$$

This setup leads to a crack initiation in the bulk. The crack then propagates to the top surface resulting in an arch like fracture line. Intermediate steps of the computation are reported in Fig. 38. The plots in Fig. 38 are computed by a discretization of 100×100 elements. The results are obtained by standard 4-node finite elements with bi-linear shape functions. The same spatial interpolation is used for u, v and s. The time integration of (6.7) is done by an implicit/backward Euler scheme using adaptive time step control. The initial time step is set to $\Delta t = 0.01$. The time step Δt is halved if the Newton method for the increments does not converge in 8 iterations. This time step halving is repeated at most 10 times. The time step Δt is increased to twice its value if 4 or less Newton iterations are required.Using n elements along the edges a and b, the number of degrees of freedom (d.o.f.) is reported in Table 30. The monolithic solution strategy was used. As a quantitative result the overall reaction force F in y-direction on the segment (D)

$$F = \int_{A(\mathrm{D})} \sigma_{yy} \, \mathrm{d}A \tag{6.20}$$

is reported with respect to the displacement v in Fig. 39.

7 Quasi-Static Pressure-Driven Cavity

7.1 Introduction

In this benchmark, we consider a lower-dimensional fracture in a d-dimensional domain. For the time being we restrict ourselves to $d = 2$. This fracture has a constant length and varying width (also known in the literature as aperture, crack opening displacement or COD). The driving force is a given constant pressure prescribed in the fracture. The setting is motivated by the book of Sneddon and Lowengrub [48] and therefore known as 'Sneddon' benchmark or 'pressure-driven cavity'. Analytical solutions are derived in Sneddon and Lowengrub [48] and are also discussed in [49]. Subsequently, [50, 51] coin the proposed benchmark, and provide numerical results.

7.2 Equations

In this section, we introduce the used notation and state the governing equations. In the following, the L^2 product is denoted as $(\cdot, \cdot)$:

$$(x, y) := \int_\Omega x \cdot y \, d\Omega,$$

and for vector-valued quantities by

$$(X, Y) := \int_\Omega X : Y \, d\Omega.$$

The domain $\Omega \subset \mathbb{R}^d$ ($d = 2$ for the 2D benchmark problem) is an open, connected and bounded set. The crack C is a one-dimensional set contained in Ω.

7.2.1 The Energy Formulation

The Francfort-Marigo functional [44] describes the energy of a crack in an elastic medium as

$$E(u, C) = \frac{1}{2}(\sigma, e(u)) - \int_C \tau \cdot u \, \mathrm{d}s + G_C \mathcal{H}^1(C), \tag{7.1}$$

where $u : \Omega \to \mathbb{R}^d$ is the vector-valued displacement function and $\sigma = \sigma(u)$ the classical stress tensor of linearized elasticity defined as

$$\sigma(u) := 2\mu e(u) + \lambda \mathrm{tr}(e(u))I,$$

with the Lamé parameters $\mu, \lambda > 0$. The symmetric strain tensor $e(u)$ is defined as

$$e(u) := \frac{1}{2}(\nabla u + \nabla u^T).$$

The energy functional E consists of three terms: a bulk energy term, a traction energy, and a crack energy contribution. Specifically, traction forces are denoted by τ. The critical energy release rate is denoted by $G_C > 0$. The term $\mathcal{H}^1(C)$ stands for the Hausdorff measure denoting the length of the crack.

Combining this notation with the poro-elastic stress $\sigma_{\mathrm{poro}} = \sigma - \alpha p I$ with the Biot coefficient $\alpha \in [0, 1]$ and

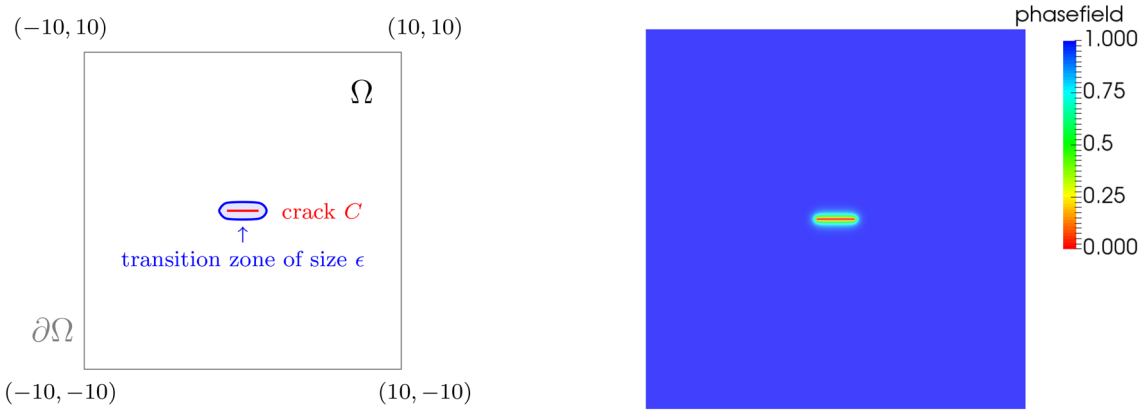

Fig. 40 Domain Ω (in 2D) with Dirichlet boundaries $\partial\Omega$, an initial crack C of length $2l_0$ and a zone of width ϵ, where the phase-field function φ is defined

including the phase-field variable φ, we get the following energy functional Mikelić et al. [52]:

$$E(u, C) = \frac{1}{2}(\sigma, e(u)) - (\alpha - 1)(\varphi^2 p, \mathrm{Div} u) + (\varphi^2 \nabla p, u) + G_C \mathcal{H}^1(C),$$

where $p : \Omega \to \mathbb{R}$ is a given pressure.

Remark 1 The considered benchmark setting in this study is posed in an elastic medium. For this reason, we set $\alpha = 0$. Moreover, a constant pressure is applied, and therefore the pressure gradient is zero, i.e., $\nabla p = 0$. This yields the simplified energy functional

$$E(u, C) = \frac{1}{2}(\sigma, e(u)) + (\varphi^2 p, \mathrm{Div} u) + G_C \mathcal{H}^1(C),$$

which is used in the following.

Following Bourdin et al. [45], the crack C is approximated by a continuous phase-field variable $\varphi : \Omega \to [0, 1]$, which is zero in the crack and one in the unbroken solid with a transition zone with size $\epsilon > 0$. The regularization parameter $\epsilon > 0$ allows control of the diffusive transition zone. So the crack surface energy $G_C \mathcal{H}^1(C)$ in Eq. (7.1) can be reformulated to an elliptic Ambrosio-Tortorelli functional, which yields:

Formulation 1 (Regularized energy functional for pressurized fractures)

$$E_\epsilon(u, \varphi) = \frac{1}{2}\Big(\big((1 - \kappa)\varphi^2 + \kappa\big)\sigma(u), e(u)\Big) + (\varphi^2 p, \mathrm{Div} u) + G_C\Big(\frac{1}{2\epsilon}\|1 - \varphi\|^2 + \frac{\epsilon}{2}\|\nabla\varphi\|^2\Big),$$

where κ is a positive regularization parameter for the elastic energy with $\kappa \ll \epsilon$.

Formulation 2 (Fracture energy minimization under constraint) Find functions u and φ for almost all times t with

$$\min E_\epsilon(u, \varphi) \quad \text{s. t. } \partial_t \varphi \le 0. \tag{7.2}$$

The constraint realizes the crack irreversibility. Physically-speaking: the crack cannot heal. To derive an incremental version, the constraint is discretized in time via:

$$\frac{\varphi(t^{n+1}) - \varphi(t^n)}{t^{n+1} - t^n} \le 0.$$

Remark 2 We notice that this benchmark setting is a stationary test case. Due to the crack irreversibility constraint, we compute a few time step solutions in order to converge to this stationary limit.

7.2.2 The Weak Formulation

Our weak formulation is based on [51]. With

$$V := H_0^1(\Omega),$$
$$W_{\text{in}} := \{w \in H^1(\Omega) | w \le \varphi^{n-1} \le 1 \text{ a.e. on } \Omega\}, \quad \text{and}$$
$$W := H^1(\Omega),$$

we obtain the following weak formulation of Eq. (7.2).

Formulation 3 (Euler–Lagrange System of Formulation 2) *Find $(u, \varphi) \in V \times W$ with*

$$\Big(\big((1 - \kappa)\varphi^2 + \kappa\big)\sigma(u), e(w)\Big) + (\varphi^2 p, \mathrm{Div} w) = 0 \quad \forall w \in V,$$

and

$$(1-\kappa)(\varphi\sigma(u) : e(u), \psi-\varphi) + 2(\varphi p \mathrm{Div} u, \psi-\varphi) + G_C\Big(-\frac{1}{\epsilon}(1-\varphi, \psi-\varphi) + \epsilon(\nabla\varphi, \nabla(\psi-\varphi))\Big) \geq 0 \quad \forall \psi \in W_{\text{in}} \cap L^\infty(\Omega).$$

7.3 A 2D Pressurized Fracture

The theoretical calculations of Sneddon [53] and Sneddon and Lowengrub [48] form the basis of this example. All settings to simulate the benchmark of the given pressurized fracture problem are listed in the following sections.

7.3.1 Setup

7.3.1.1 Domain Definition The two-dimensional domain $\Omega = (-10, 10)^2$ is sketched in Fig. 40.

7.3.1.2 Initial Conditions An initial crack with length $2l_0 = 2.0$ and thickness d of two cells on $\Omega_c = [-1, 1] \times [-d, d] \subset \Omega$ is prescribed by help of the phase-field function φ, i.e., $\varphi = 0$ in Ω_c and $\varphi = 1$ in $\Omega \setminus \Omega_c$. Note that the thickness of $2d$ corresponds to $2h/\sqrt{2}$.

7.3.1.3 Boundary Conditions As boundary conditions, the displacements u are set to zero on $\partial\Omega$. For the phase-field variable, we use homogeneous Neumann conditions (traction free), i.e., $\epsilon\partial_n\varphi = 0$ on $\partial\Omega$.

7.3.1.4 Parameter Settings The determined parameter values are listed in Table 31.

If it is of interest to compute the exact values of the Lamé coefficients λ and μ, the converting formulae are: $\lambda = \frac{\nu E}{(1+\nu)(1-2\nu)}$ and $\mu = \frac{E}{2(1+\nu)}$.

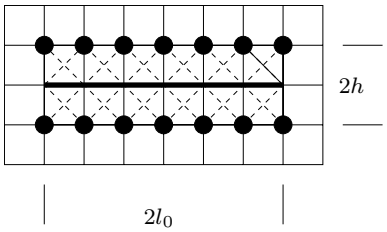

Fig. 41 Zoom-in to the center of the domain Ω. The lower-dimensional crack with length $2l_0 = 2.0$ (middle line in black) is approximated as a volume by extending it by one cell in normal up and down direction

Table 31 Setting of the benchmark and numerical parameters in 2D

Parameter	Definition	Value
Ω	Domain	$(-10, 10)^2$
h	cell diameter (diagonal)	
l_0	Half crack length	1.0
G_c	Fracture toughness	1.0
E	Young's modulus	1.0
ν	Poisson's ratio	0.2
p	Injected pressure	10^{-3}
TOL_t	Tolerance time step loop	10^{-5}
ϵ	Bandwidth of the crack	$4h$
κ	Regularization parameter	0

7.3.2 Quantities of Interest

As benchmark comparisons, we propose the following quantities of interest:

1. Section 7.3.2.1: Crack opening displacement (COD) as a function of the x coordinate;
2. Section 7.3.2.2: The maximal $\mathrm{COD}_{\max}$ in the middle of the fracture;
3. Section 7.3.2.3: Total volume of the crack (TCV);
4. Section 7.3.2.4: Bulk energy;
5. Section 7.3.2.5: Crack energy.

For the COD, $\mathrm{COD}_{\max}$ and TCV, manufactured reference values can be computed for a infinite domain from the formulae presented in [48, Section 2.4]. We restate the corresponding formulae below and provide the reference values for our proposed material, and model parameters. In our comparisons, the reference values on an infinite domain are denoted by `reference Sneddon`. Additionally, we provide values based on fine computations on adaptively refined meshes for the finite domain. See Heister and Wick [54] for more details about the used method. These reference values are denoted by `reference adaptive`. Here, we also calculate the errors between the `reference adaptive` solution and our numerical results. These errors are 'relative' errors computed via

$$\frac{|\texttt{numerical result} - \texttt{reference adaptive}|}{|\texttt{reference adaptive}|}.$$

7.3.2.1 Crack Opening Displacement The width or crack opening displacement (COD) under spatial mesh refinement can be measured in the numerical tests. The width is defined as

$$\mathrm{COD}(x) := [u \cdot n](x) \approx \int_{-\infty}^{\infty} u(x, y) \cdot \nabla\varphi(x, y)\, \mathrm{d}y, \tag{7.3}$$

where $x \in [-1, 1]$ the x-coordinate along the integral in y direction. The reference value for a infinite domain (cf. Sneddon and Lowengrub [48]) is given by:

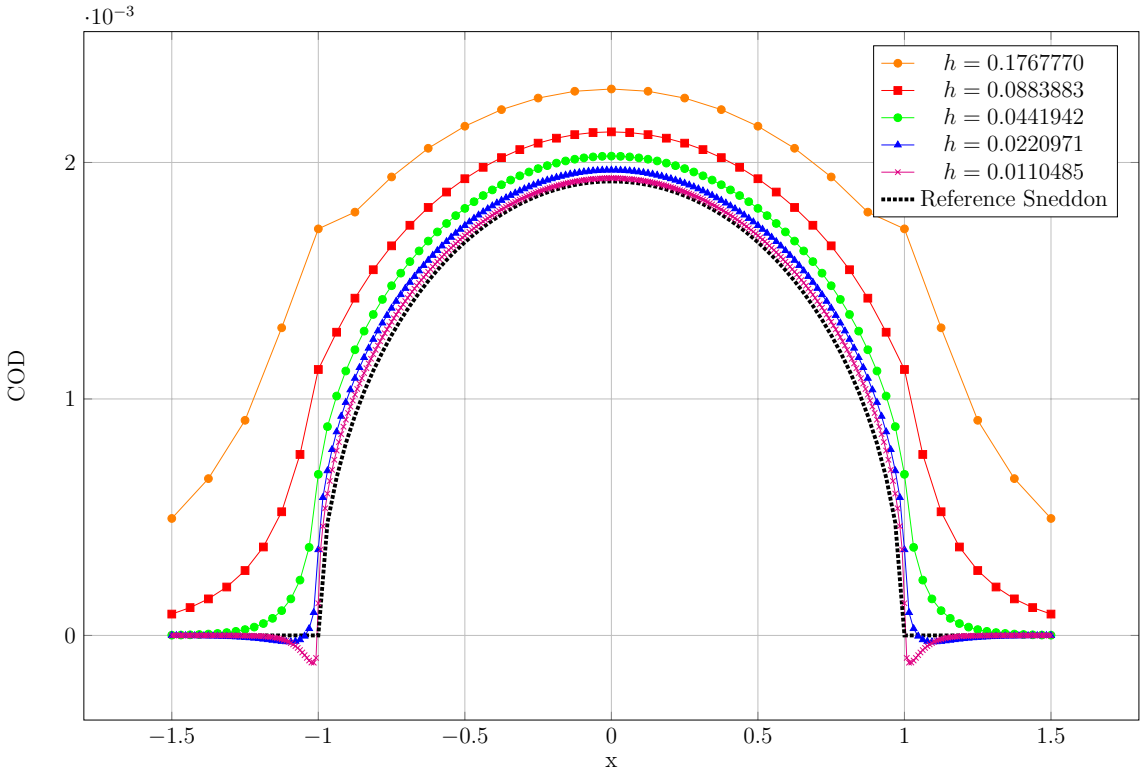

Fig. 42 Benchmark 6: crack opening displacements (COD) for various refinement levels

$$\begin{aligned} \mathrm{COD}_{\mathrm{ref}}(x) &= 2\frac{pl_0}{E'}\left(1-\frac{x^2}{l_0^2}\right)^{1/2} \\ &= 1.92\times 10^{-3}\left(1-\frac{x^2}{l_0^2}\right)^{1/2}, \end{aligned} \tag{7.4}$$

where p is the applied pressure, l_0 is the half crack length and $E' := \frac{E}{1-\nu^2}$.

7.3.2.2 Maximum Crack Opening Displacement We evaluate the COD in the middle of the fracture (due to symmetry the maximum is attained at $x = 0$):

$$\mathrm{COD}_{\max} := [u\cdot n](0) \approx \int_{-\infty}^{\infty} u(0,y)\cdot\nabla\varphi(0,y)\,\mathrm{d}y.$$

7.3.2.3 Total Crack Volume The total crack volume (TCV) can be computed numerically using

Table 32 Benchmark 6: numerical $\mathrm{COD}_{\max}$ values for five refinement levels in 2D and respectively the error to reference values based on an adaptively refined mesh Heister and Wick [54]

DoF	h	$\mathrm{COD}_{\max}$	Rel. error to adapt.
77,763	0.1767770	2.31073×10^{-3}	0.22166
309,123	0.0883883	2.12944×10^{-3}	0.12581
1,232,643	0.0441942	2.02688×10^{-3}	0.07159
4,922,883	0.0220971	1.96789×10^{-3}	0.04040
19,676,163	0.0110485	1.93355×10^{-3}	0.02225
Reference adaptive Heister and Wick [54]	–	1.89147×10^{-3}	–
Reference Sneddon on Ω_∞	–	1.92000×10^{-3}	–

For comparison, the exact $\mathrm{COD}_{\max}$ given by Sneddon and Lowengrub (Reference Sneddon) for an infinite domain is listed

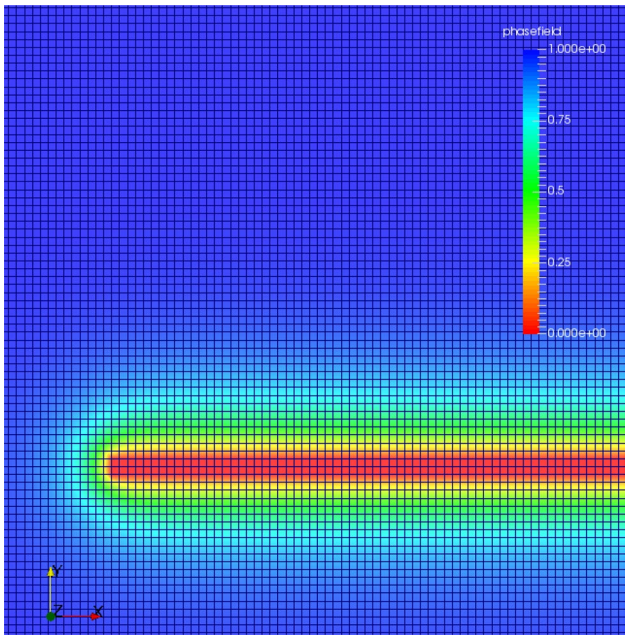

Fig. 43 Benchmark 6: a zoom of the left half of the pressurized fracture based on the setup in 2D with 7 refinements: 4,922,883 degrees of freedom, $h = 0.0220971$

$$\mathrm{TCV}_{h,\epsilon} = \int_\Omega u(x,y) \cdot \nabla\varphi(x,y)\,\mathrm{d}(x,y). \tag{7.5}$$

A formula for the limit can be obtained using Sneddon and Lowengrub [48]. Using symmetry of the configuration, i.e., $u_y(x,0^+) = -u_y(x,0^-)$, and the known crack location $[-1,1]\times\{0\}$, one obtains

$$\mathrm{TCV}_{2D} = 2\int_{-\infty}^{\infty} u_y(x,0^+)\,\mathrm{d}x,$$

where $0^\pm$ denotes the respective limit from above or below, and u_y denotes the second (y) component of the displacement.

Using the exact representation of u_y (cf. Sneddon and Lowengrub [48], page 29)

$$u_y(x,0^+) = \frac{pl_0}{E'}\left(1 - \frac{x^2}{l_0^2}\right)^{1/2}$$

we obtain:

$$\mathrm{TCV}_{2D} = \int_{-\infty}^{\infty} 2u_y(x,0^+)\,\mathrm{d}x = \frac{2\pi p l_0^2}{E'}. \tag{7.6}$$

Applied to our parameter settings, we consequently obtain the reference value for an infinite domain as:

$$\mathrm{TCV}_{2D} \approx 6.03186 \times 10^{-3}.$$

In the following, the formula to compute bulk and crack energy as two further numerical quantities of interest are given.

7.3.2.4 Bulk Energy Next, we compute the bulk energy E_B given by

$$E_B = \int_\Omega ((1-\kappa)\varphi^2 + \kappa)\psi(e)\,\mathrm{d}(x,y). \tag{7.7}$$

The strain energy functional $\psi(e)$ in Eq. (7.7) is defined as

$$\psi(e) := \mu\mathrm{tr}(e(u)^2) + \frac{1}{2}\lambda\mathrm{tr}(e(u))^2.$$

Here, no manufactured reference values are provided and we only present values computed numerically.

7.3.2.5 Crack Energy Finally, we compute the crack energy

$$E_C = \frac{G_C}{2}\int_\Omega \left(\frac{(\varphi-1)^2}{\epsilon} + \epsilon|\nabla\varphi|^2\right)\mathrm{d}(x,y). \tag{7.8}$$

Again, no manufactured reference values are provided and we only present values computed numerically.

Table 33 Benchmark 6: total crack volume for five refinement levels in 2D and respectively the error to reference values based on an adaptively refined mesh (Reference adaptive) Heister and Wick [54]

DoF	h	TCV	Rel. error to adapt.
77,763	0.1767770	11.31650×10^{-3}	0.90536
309,123	0.0883883	8.18239×10^{-3}	0.37767
1,232,643	0.0441942	6.91774×10^{-3}	0.16474
4,922,883	0.0220971	6.39662×10^{-3}	0.07699
19,676,163	0.0110485	6.16564×10^{-3}	0.03810
Reference adaptive Heister and Wick [54]	–	5.93930×10^{-3}	–
Reference Sneddon on Ω_∞	–	6.03186×10^{-3}	–

For comparison we include the exact TCV given by Sneddon and Lowengrub for an infinite domain

Table 34 Benchmark 6: bulk and crack energy for five refinement levels in 2D

DoF	h	Bulk energy	Rel error	Crack energy	Rel. error
77,763	0.1767770	5.86652×10^{-6}	0.9746	3.43192	0.4566
309,123	0.0883883	4.06538×10^{-6}	0.3684	2.89463	0.2285
1,232,643	0.0441942	3.38745×10^{-6}	0.1402	2.62540	0.1143
4,922,883	0.0220971	3.13916×10^{-6}	0.0566	2.49078	0.0571
19,676,163	0.0110485	3.04430×10^{-6}	0.0247	2.42347	0.0286
Reference adaptive Heister and Wick [54]	–	2.97093×10^{-6}	–	2.35616	–

Relative error with respect to adaptively refined mesh (Reference adaptive) Heister and Wick [54]

7.4 Numerical Results for the 2D Benchmark

7.4.1 Solution Approaches

We use H^1 conforming finite elements on quadrilaterals (2D). Specifically, we use bilinear elements Q_1^c Ciarlet [55] for both, the displacements and the phase-field variable. In accordance with Heister et al. [51], a monolithic approach with an extrapolation of the phase-field variable in the displacement equation is used.

To treat the variational inequality, we employ a primal-dual active set method (again following [51]) with the recent open-source code published in Heister and Wick [54] based on deal.II Arndt et al. [56]. Furthermore, we emphasize that in this benchmark setting we exclusively use uniform mesh refinement.

The benchmark is sensitive to how the phase field variable is initialized from the given initial condition in 7.3.1.2. We use nodal interpolation[1] of the piecewise bi-linear finite element variable as shown in Fig. 41. Using an L^2 projection (or any other form of projection) instead, yields slightly different benchmark results.

The overall nonlinear discrete problem is then solved with a Newton method in which (when necessary), globalization is achieved with a simple backtracking line search method.

The code for the benchmarks performed here, again based on the Finite Element library deal.II Arndt et al. [56], is available at https://github.com/tjhei/cracks/tree/sneddon_spp_benchmark including all necessary parameter files.

7.4.2 Numerical Results

In the following sections all numerical results for the determined quantities of interest are given and compared to reference values.

We start the computation with a structured mesh of 10 by 10 cells, where each cell has an extent of 2 by 2 units and a diameter $h = \sqrt{8} \approx 2.828$. From there, we refine the mesh globally, cutting the size of each cell by a factor of 2 in each step.

Remark 3 Keep in mind that the reference values of COD and TCV in the previous section are valid for $\epsilon = 0$ and for an infinite domain Ω_∞. While we can expect convergence of the results presented here against the reference values with $\epsilon \to 0$, the problem is still given on a finite domain. Therefore, convergence against these reference values can not be expected.. Instead, we compare with with numerical results on the same finite domain but on very fine, adaptively refined meshes from Heister and Wick [54]. The reference values from Sneddon/Lowengrub are denoted as `Reference Sneddon`, while the numerical reference values are denoted as `Reference adaptive`.

7.4.2.1 COD (Quantity of Interest No. 1) Figure 42 shows the crack opening displacements (COD), computed with Eq. (7.3), over the width of the crack for several tests with different sizes of the mesh size parameter h. The computations correspond to 4 to 8 global refinements of the initial mesh. The dotted black line gives the exact COD values from Eq. (7.4).

7.4.2.2 Maximum COD (Quantity of Interest No. 2) To compare the COD values at one fixed point, in Table 32 the values of COD_{max} using Eq. (7.3) are listed and the (relative) error of the numerical COD value in comparison to the computed value on an adaptively refined mesh (`Reference adaptive`). A zoom on the pressurized fracture is given in Fig. 43.

7.4.2.3 Total Crack Volume (Quantity of Interest No. 3) In Table 33, the computed values of the total crack volume Eq. (7.5) are provided for five mesh refinement levels and compared to the exact TCV value Eq. (7.6).

7.4.2.4 Bulk and Crack Energies (Quantity of Interest No. 4 and No. 5) For the bulk and crack energy no reference values are provided. Here, in Table 34, the bulk and crack energy values are shown for five mesh refinement levels using the definitions of Eqs. (7.7) and (7.8), respectively.

[1] In deal.II done using VectorTools:interpolate().

8 Conclusion

In the first two benchmarks we provided results on hyperelastic and elasto-plastic problems at finite strains. Different (mixed) finite element technologies as well as *p*-FEM was used in order to obtain convergent results for certain displacement and stress values for the Cook's membrane and an incompressible block problem. In benchmark problem in Sect. 4, the convergence behavior of a thin as well as a thick plate with a distributed load was investigated. Two different finite element technologies, namely solid and solid-shell were applied in addition to the standard Q1 finite element formulation. It was shown that due to the shell structure of the problem, the standard finite element method observes severe locking whereas the other methods show an outstanding convergence rate with respect to the mesh refinement. In the fourth benchmark, material interfaces were considered. Therein, two discretization methods, finite elements and isogeometric analysis are compared, which show very good agreements for various inclusion configurations. In the fifth benchmark, a phase-field fracture method was applied to two settings. First a three dimensional configuration and then a two-dimensional setting. As quantity of interest, displacement-reaction curves were adopted. In the last benchmark, a pressurized fracture in elasticity was considered for which numerical and manufactured reference values were generated. Moreover, some codes are open-source to reproduce the presented findings. All benchmarks shall serve as future reference for other discretization methods and other numerical solution algorithms.

Acknowledgements The authors gratefully acknowledge the support by the Deutsche Forschungsgemeinschaft in the Priority Program 1748 "Reliable simulation techniques in solid mechanics. Development of non- standard discretization methods, mechanical and mathematical analysis" under the projects 'Coordination Funds'—project number 255431921 (SCHR 570/23-1&2), 'Novel finite elements—Mixed, Hybrid and Virtual Element formulations at finite strains for 3D applications'—project number 255431921 (SCHR 570/23-1&2, WR 19/50-1&2), 'Approximation and Reconstruction of Stresses in the Deformed Configuration for Hyperelastic Material Models'—project number 392587488 (SCHR 570/34-1), 'First-order system least squares finite elements for finite elasto-plasticity'—project number 255798245 (SCHW 1355/2-1, SCHR 570/24-1), 'Hybrid discretizations in solid mechanics for non-linear and non-smooth problems'—project number 643861 (RE 1057/30-1&2), 'High-order immersed-boundary methods in solid mechanics for structures generated by additive processes'—project number 255496529 (DU 405/8-1&2, RA 624/27-1&2, SCHR 1244/4-1&2), 'Adaptive isogeometric modeling of discontinuities in complex-shaped heterogeneous solids'—project number 255853920 (KA 3309/3-1&2), 'Advanced Finite Element Modelling of 3D Crack Propagation by a Phase Field Approach' - project number 255846293 (MU1370/11-1&2 and KU 3221/1-1&2), 'Structure Preserving Adaptive Enriched Galerkin Methods for Pressure-Driven 3D Fracture Phase-Field Models'—project number 392587580 (WA 4200/1-1, WI 4367/2-1, and WO 1936/5-1), Timo Heister was partially supported by the National Science Foundation (NSF) Award DMS-2028346, OAC-2015848, EAR-1925575, by the Computational Infrastructure in Geodynamics initiative (CIG), through the NSF under Award EAR-0949446 and EAR-1550901 and The University of California—Davis, and by Technical Data Analysis, Inc. through US Navy STTR Contract N68335-18-C-0011. Clemson University is acknowledged for generous allotment of compute time on Palmetto cluster (Sect. 7).

Funding Open Access funding provided by Projekt DEAL.

References

1. Cook RD (1974) Improved two-dimensional finite element. J Struct Div 100:1851–1863
2. Boffi D, Brezzi F, Fortin M (2013) Mixed finite element methods and applications. Springer, North Holland
3. Szabó BA, Babuška I (1991) Finite element analysis. Wiley, New York
4. Düster A, Rank E, Szabó B (2017) The p-version of the finite element and finite cell methods. In: Stein E, de Borst R, Hughes TJR (eds) Encyclopedia of computational mechanics. Part 1: solids and structures, chapter 4, 2nd edn. Wiley, Hoboken, pp 137–171
5. Ciarlet PG (1988) Mathematical elasticity, volume 1: three dimensional elasticity. Elsevier Science Publishers B.V, North Holland
6. Hartmann S, Neff P (2003) Polyconvexity of generalized polynomial-type hyperelastic strain energy functions for near-incompressibility. Int J Solids Struct 40:2767–2791
7. Netz T, Düster A, Hartmann S (2013) High-order finite elements compared to low-order mixed element formulations. ZAMM-Zeitschrift für Angewandte Mathematik und Mechanik 93(2–3):163–176
8. Düster A, Hartmann S, Rank E (2003) p-FEM applied to finite isotropic hyperelastic bodies. Comput Methods Appl Mech Eng 192:5147–5166
9. Wriggers P (2008) Nonlinear finite-element-methods. Springer, Berlin. ISBN 3-540-71000-0
10. Simo JC (1988) A framework for finite strain elastoplasticity based on maximum plastic dissipation and the multiplicative decomposition. Part I: continuum formulation. Comput Methods Appl Mech Eng 66:199–219
11. Simo JC (1992) Algorithms for static and dynamic multiplicative plasticity that preserve the classical return mapping schemes of the infinitesimal theory. Comput Methods Appl Mech Eng 68:61–112
12. Simo JC (1998) Numerical analysis and simulation of plasticity. In: Ciarlet PG, Lions JL (eds) Handbook of numerical analysis, vol 6. Elsevier, Amsterdam, pp 183–499
13. Simo JC, Miehe C (1992) Associative coupled thermoplasticity at finite strains: formulation, numerical analysis and implementation. Comput Methods Appl Mech Eng 98:41–104

14. Korelc J, Stupkiewicz S (2014) Closed-form matrix exponential and its application in finite-strain plasticity. Int J Numer Meth Eng 98:960–987
15. Weber G, Anand L (1990) Finite deformation constitutive equations and a time integration procedure for isotropic, hyperelastic-viscoplastic solids. Comput Methods Appl Mech Eng 79:173–202
16. Eterovic AL, Bathe KJ (1990) A hyperelastic-based large strain elasto-plastic constitutive formulation with combined isotropic-kinematic hardening using the logarithmic stress and strain measures. Int J Numer Methods Eng 30:1099–1114
17. Korelc J (1997) Automatic generation of finite-element code by simultaneous optimization of expressions. Theor Comput Sci 187:231–248
18. Korelc J (2002) Multi-language and multi-environment generation of nonlinear finite element codes. Eng Comput 18:312–327
19. Korelc J, Wriggers P (2016) Automation of finite element methods. Springer, Cham
20. Düster A, Kollmannsberger S (2010) AdhoC^4—user's guide. Lehrstuhl für Computation in Engineering, TU München, Numerische Strukturanalyse mit Anwendungen in der Schiffstechnik, TU Hamburg-Harburg
21. Reese S, Wriggers P, Reddy BD (2000) A new locking-free brick element technique for large deformation problems in elasticitys. Comput Struct 74:291–304
22. Simo JC, Armero F (1992) Geometrically non-linear enhanced strain mixed methods and the method of incompatible modes. Int J Numer Meth Eng 33:1413–1449
23. Mueller-Hoeppe DS, Loehnert S, Wriggers P (2009) A finite deformation brick element with inhomogeneous mode enhancement. Int J Numer Meth Eng 78:1164–1187
24. Korelc J, Šolinc U, Wriggers P (2010) An improved EAS brick element for finite deformation. Comput Mech 46:641–659
25. Szabó B, Düster A, Rank E (2004) The p-version of the finite element method. In: Stein E (ed) Encyclopedia of computational mechanics. Wiley, Hoboken. ISBN 978-0-470-09135-7
26. Reese S, Wriggers P (2000) A stabilization technique to avoid hourglassing in finite elasticity. Int J Numer Methods Eng 48:79–109
27. Bayat HR, Krämer J, Wunderlich L, Wulfinghoff S, Reese S, Wohlmuth B, Wieners C (2018) Numerical evaluation of discontinuous and nonconforming finite element methods in nonlinear solid mechanics. Comput Mech 62:1413–1427
28. Bayat HR, Wulfinghoff S, Kastian S, Reese S (2018) On the use of reduced integration in combination with discontinuous Galerkin discretization: application to volumetric and shear locking problems. Adv Model Simul Eng Sci 5:1–16
29. Reese S (2005) On a physically stabilized one point finite element formulation for three-dimensional finite elasto-plasticity. Comput Methods Appl Mech Eng 194:4685–4715
30. Schwarze M, Reese S (2009) A reduced integration solid-shell finite element based on the EAS and the ANS concept—geometrically linear problems. Int J Numer Methods Eng 80:1322–1355
31. Schwarze M, Reese S (2011) A reduced integration solid-shell finite element based on the EAS and the ANS concept—large deformation problems. Int J Numer Methods Eng 85:289–329
32. Reese S, Bayat HR, Wulfinghoff S (2017) On an equivalence between a discontinuous Galerkin method and reduced integration with hourglass stabilization for finite elasticity. Comput Methods Appl Mech Eng 325:175–197
33. Düster A, Rank E, Szabó BA (2017) The p-version of the finite element method and finite cell methods. In: Stein E, Borst R, Hughes TJR (eds) Encyclopedia of computational mechanics, vol 2. Wiley, Chichester, pp 1–35 ISBN 978-1-119-00379-3
34. Joulaian M, Düster A (2013) Local enrichment of the finite cell method for problems with material interfaces. Comput Mech 52(4):741–762
35. Hennig P, Maier R, Peterseim D, Schillinger D, Verfürth B, Kästner M (2019) A diffuse modeling approach for embedded interfaces in linear elasticity. GAMM-Mitteilungen
36. Elhaddad M, Zander N, Bog T, Kudela L, Kollmannsberger S, Kirschke J, Baum T, Ruess M, Rank E (2017) Multi-level hp-finite cell method for embedded interface problems with application in biomechanics. Int J Numer Methods Biomed Eng 34(4):e2951
37. Cottrell JA, Hughes TJR, Reali A (2007) Studies of refinement and continuity in isogeometric structural analysis. Comput Methods Appl Mech Eng 196(41–44):4160–4183
38. Szabó BA, Babuška I (1991) Finite element analysis. Wiley, New York. ISBN 0-471-50273-1
39. Hennig P, Müller S, Kästner M (2016) Bézier extraction and adaptive refinement of truncated hierarchical NURBS. Comput Methods Appl Mech Eng 305:316–339
40. Hennig P, Kästner M, Morgenstern P, Peterseim D (2017) Adaptive mesh refinement strategies in isogeometric analysis—a computational comparison. Comput Methods Appl Mech Eng 316:424–448
41. Sukumar N, Chopp DL, Moës N, Belytschko T (2001) Modeling holes and inclusions by level sets in the extended finite-element method. Comput Methods Appl Mech Eng 190(46–47):6183–6200 ISSN 0374-2830
42. Yosibash Z (1997) Numerical analysis on singular solutions of the poisson equation in two-dimensions. Comput Mech 20(4):320–330 ISSN 1432-0924
43. Kellogg RB (1974) On the poisson equation with intersecting interfaces. Appl Anal 4(2):101–129
44. Francfort GA, Marigo J-J (1998) Revisiting brittle fracture as an energy minimization problem. J Mech Phys Solids 46(8):1319–1342
45. Bourdin B, Francfort G, Marigo J-J (2000) Numerical experiments in revisited brittle fracture. J Mech Phys Solids 48(4):797–826
46. Bourdin B (2007) Numerical implementation of the variational formulation for quasi-static brittle fracture. Interfaces Free Bound 9:411–30
47. Kuhn C (2012) Numerical and analytical investigation of a phase field model for fracture. PhD thesis, Technische Universität Kaiserslautern
48. Sneddon IN, Lowengrub M (1969) Crack problems in the classical theory of elasticity. Wiley, New York
49. Bourdin B, Chukwudozie CP, Yoshioka K et al (2012) A variational approach to the numerical simulation of hydraulic fracturing. In: SPE annual technical conference and exhibition. Society of Petroleum Engineers
50. Wheeler MF, Wick T, Wollner W (2014) An augmented-Lagrangian method for the phase-field approach for pressurized fractures. Comput Methods Appl Mech Eng 271:69–85
51. Heister T, Wheeler MF, Wick T (2015) A primal-dual active set method and predictor-corrector mesh adaptivity for computing fracture propagation using a phase-field approach. Comput Methods Appl Mech Eng 290:466–495
52. Mikelić A, Wheeler MF, Wick T (2019) Phase-field modeling through iterative splitting of hydraulic fractures in a poroelastic medium. GEM Int J Geomath 10(1):2
53. Sneddon IN (1946) The distribution of stress in the neighbourhood of a crack in an elastic solid. Proc R Soc Lond A 187(1009):229–260
54. Heister T, Wick T (2018) Parallel solution, adaptivity, computational convergence, and open-source code of 2d

and 3d pressurized phase-field fracture problems. PAMM 18(1):e201800353
55. Ciarlet PG (2002) The finite element method for elliptic problems. Society for Industrial and Applied Mathematics, Philadelphia
56. Arndt D, Bangerth W, Clevenger TC, Davydov D, Fehling M, Garcia-Sanchez D, Harper G, Heister T, Heltai L, Kronbichler M, Kynch RM, Maier M, Pelteret J-P, Turcksin B, Wells D (2019) The `deal.II` library, version 9.1. J Numer Math 27(4):203–213